Zonation of Hydrogen in Kimberlitic and Mantle Olivines: A Possible Proxy for the Water Content of Kimberlite Magmas

by

Luke Hilchie

Submitted in partial fulfilment of the requirements
for the degree of Master of Science

at

Dalhousie University
Halifax, Nova Scotia
August 2011

DALHOUSIE UNIVERSITY

DEPARTMENT OF EARTH SCIENCES

The undersigned hereby certify that they have read and recommend to the Faculty of Graduate Studies for acceptance a thesis entitled “Zonation of Hydrogen in Kimberlitic and Mantle Olivines: A Possible Proxy for the Water Content of Kimberlite Magmas” by Luke Hilchie in partial fulfilment of the requirements for the degree of Master of Science.

Dated: August 8, 2011

Supervisor: _____

Readers: _____

_____

_____

_____

DALHOUSIE UNIVERSITY

DATE: August 8, 2011

AUTHOR: Luke Hilchie

TITLE: Zonation of Hydrogen in Kimberlitic and Mantle Olivines: A Possible Proxy for the Water Content of Kimberlite Magmas

DEPARTMENT OR SCHOOL: Department of Earth Sciences

DEGREE: MSc CONVOCATION: October YEAR: 2011

_____

Signature of Author

For my wife Ashley.

I hope I was at least half as helpful to you when you wrote your thesis as you were to me.

Table of Contents

List of Tables

List of Figures

Abstract

Volatiles are fundamental to many aspects of kimberlite magmatism. However, the volatile compositions and concentrations are poorly defined. Enrichment of H in kimberlitic olivines, many of which are xenocrysts, suggests high water content, but the extent to which H exchanges between these xenocrysts and kimberlite magmas remains unclear. This study investigates zonation of H in kimberlite-hosted xenolith and macrocrystic olivines using Fourier transform infrared spectroscopy to constrain the extent of re-equilibration. Data show that, depending on locality, xenolith olivines exhibit either no H-zonation, or substantial H-depletion in their rims. Macrocrysts feature similar trends to xenolith olivines from the same intrusion. In terms of the rim:core ratio of H, strongly zoned olivines average ~0.5, whereas poorly zoned olivines average at ~0.9 (macrocrysts) or 1.0 (xenolith olivines). Locality-specific H-zonation could result from different magmatic thermal regimes, water concentrations, or ascent durations. If the magmas that contained weakly zoned olivines were anhydrous, their restricted zoning requires ascent durations (< 20 min at 1100 °C) that are considerably shorter than published estimates (~1-24 hr at 1100 °C). These findings suggest that elevated magmatic water concentrations minimized loss of H from olivine in these kimberlites, showing that non-equilibrated xenocrysts could indirectly record high water concentrations in the form of weak H-zonation. Strong H-depletion patterns in olivines from other kimberlites may reflect lower initial magmatic water concentrations, or loss of fluid to country rocks. Future studies could compare H-zonation to temperature and ascent rate estimates, and field relationships to better elucidate the causes of locality-specific H-zonation. An apparent correlation between diamond grade and H-zonation warrants further investigation.

List of Abbreviations and Symbols Used

°C	degree Celsius
A_{int}	integrated absorbance, the area beneath peaks in an optical absorption spectrum
cm	centimeter
GPa	gigapascal
hr	hour
K	Kelvin
km	kilometer
Mg#	magnesium number, 100 · Mg/(Mg+Fe) (molar)
m	meter
min	minute
mm	millimeter
ppm	parts per million by weight
$r_{A_{int}}$	rim:core ratio of the integrated absorbance
s	second
µm	micron
vol. %	percent by volume
wt. %	percent by weight
ZAF	atomic number, absorption, fluorescence; correction scheme for raw electron microprobe data

Acknowledgements

I would like to thank a number of people whose support, encouragement, and mentorship guided me through this degree with only minor lapses in sanity, on my part.

I thank Drs. Barrie Clarke and Maya Kopylova, and BHP Billiton Diamonds Inc. for providing the samples I studied, as I could not have completed this project without them. Gordon Brown deserves special acknowledgement, as the high quality of his polished sections greatly facilitated some practical aspects of the FTIR work. I also thank Don Osburn at Acadia for manufacturing normal thin sections on short notice. I thank Dr. Thomas Stachel, whose permission to use the FTIR equipment free of charge was uncommonly generous. I also appreciate technical support from Daniel MacDonald for configuring the microprobe, and both Dan and Dr. Sergei Matveev for helping to troubleshoot some of the associated problems. I extend my gratitude to Sergei a second time for configuring the FTIR equipment. I also thank Dr. Alan Anderson for offering the use of his laboratory. Finally, I thank Dr. Jo-Anne Wartho for providing recalculations of some of her published data, which contributed to the discussion section of this thesis.

I thank my supervisory committee (Drs. Yana Fedortchouk, Sergei Matveev, Barrie Clarke, and Alan Anderson) for the support they provided throughout the degree. Alan and Barrie – I thank you both for sharing your wisdom and providing extra clarity at times when unexpected problems made planning the project difficult. Barrie – Your repeated critical reviews significantly improved my writing; I hope you find the passive voice to be absent in these unedited acknowledgements! I also value our many discussions about the more peculiar petrographic features of my samples. Sergei – Our countless e-mail discussions improved my understanding of very unfamiliar material, and helped me to frame my own views on some controversial topics. Yana – I am honoured to have served as your first graduate student, and I am grateful for the support you showed when our technical problems could have significantly delayed completion of my thesis. I keenly look forward to the future research you and your students pursue, and to future correspondence in the years to come.

I would like to thank the students and faculty in the Department of Earth Sciences, especially Jared Butler for his (unduly) self-deprecating wit, and my lab mate Zhihai Zhang for our enlightening discussions, his abundant patience, and his positive outlook on life. I also thank the students of Dr. David Hoskin (Dept. of Microbiology and Immunology), who adopted me as an unofficial lab member for many science-free occasions.

I am ever grateful to my parents, both for providing me with an excellent foundation in life, and for supporting my decision to pursue my graduate education, despite their well justified skepticism (especially you, Mum). Your financial support at different times is something I will always appreciate, but I value infinitely more the respect implicit in your approval of my choices in life.

Finally, I send endless thanks, appreciation, and love to my wife Ashley, who knows well that the words on this page cannot accurately describe how profoundly our union contributes to our lives every day. Your support, love, and reason helped me deal with the worst news, the most frustrating results, and just about any other adversity that happened upon us. I am excitedly and nervously anticipating the next stages of our lives together.

CHAPTER 1

INTRODUCTION

1.1 Volatiles and Diamonds in Kimberlites

Kimberlites are volcanic rocks derived from magmas produced at depths of ≥ 200 km, typically beneath cratons (1). As the hosts of diamonds and mantle xenoliths, kimberlites and their inclusions have received research attention disproportionate to their restricted abundance. However, significant fundamental aspects of kimberlite magmas, including their range of chemical compositions, remain matters of controversy owing to the obfuscating effects of magma contamination, ambiguous origins of included minerals, eruptive volatile loss, and late alteration (1-3). The compositions of magmas in the near-surface environment, and how they developed from primary magmas in the source region, are fundamental considerations for the origins and causes of kimberlite magmatism. Furthermore, volatiles significantly affect the physical properties of kimberlite magmas and therefore bear an important control on the dynamics (*e.g.*, eruption style, ascent rate) of their emplacement (4) and thermal evolution (5). Given that magma ascent velocity may influence the preservation of diamond xenocrysts (6-8), the amount and composition of volatiles in kimberlite magmas may have practical significance for the diamond industry. Thus, understanding records of magmatic volatiles is essential for understanding the origins, volcanology, and diamond grade (*i.e.*, mass of diamond per unit mass of rock) of kimberlites. In particular, mineralogical indicators of the behaviour of volatiles may constitute useful tools for evaluating diamond potential of new discoveries.

Determination of the concentrations of volatiles in kimberlite magmas is problematic, owing to eruptive volatile loss and addition or removal of volatiles during low temperature alteration (1, 3, 4). Resorption morphologies of diamond, which develop at high temperatures (9, 10) and depend on fluid composition and saturation (9), suggest that the fluid phase coexisting with volatile-saturated kimberlite magmas is enriched in water, as opposed to CO_2 (8). Importantly, the quality (glossiness, clarity) of diamonds from apparently volatile-undersaturated hypabyssal kimberlites is poorer than that of diamonds from volatile-saturated volcaniclastic kimberlites (8). If the inferences about

volatiles are correct, the relative concentration of magmatic water may significantly affect diamond quality. Thus, a mineralogical proxy for relative magma ascent rate *and* relative water concentration could provide insights into both the degree of diamond preservation and diamond quality.

A mineralogical proxy for diamond quality or grade can only be useful if that mineral is an abundant constituent of kimberlite. In this regard, olivine, which is the most characteristic mineral of kimberlite (2), is an ideal proxy for diamond. Although olivine is nominally anhydrous, it commonly contains trace quantities of H, making it a possible proxy for magmatic water. Indeed, H in olivine can be used to identify kimberlitic olivines in exploration samples (11), and may reflect both the diamond grade (12) and quality of diamonds in kimberlite (8). Furthermore, because H diffuses rapidly in olivine (13, 14), and its solubility drops during decompression (15, 16), the amount of H retained in olivine may reflect the ascent duration of kimberlite magma (17), which itself may control diamond preservation (6-8). Thus, H in olivine has considerable potential as a practical tool for kimberlite exploration, and evaluation of the diamond potential of new kimberlite discoveries. However, the extent to which H in olivine reflects magmatic conditions remains unclear, owing to a high proportion of xenocrystic olivine in kimberlites (1, 2, 18, 19), and contradictory evidence for exchange of H between kimberlite magma and its enclosed olivines. The following sections summarize the types and possible origins of olivine in kimberlite; expand upon the analysis, interpretation, and variation of H defects in kimberlitic olivine; and highlight the problems associated with interpretation of H in kimberlitic olivine as a magmatic proxy.

1.2 Types and Origins of Olivine in Kimberlites

Kimberlitic olivine, which comprises ~50 vol. % of hypabyssal kimberlite on average (1), includes three parageneses based crystal morphologies, according to Mitchell (2): megacrysts, macrocrysts, and phenocrysts (Fig. 1.1 A). Megacrysts are large (diameter > 10 mm), usually isolated crystals that are part of a mineralogically diverse megacrystic suite. Megacryst minerals equilibrate at some of the highest pressures determined for mantle peridotites (commonly > 4.5 GPa) (20-22), and many authors believe their crystallization is linked to production of kimberlite melts (20-24). Enrichment in incompatible elements in megacryst minerals suggests crystallization from a volatile-rich

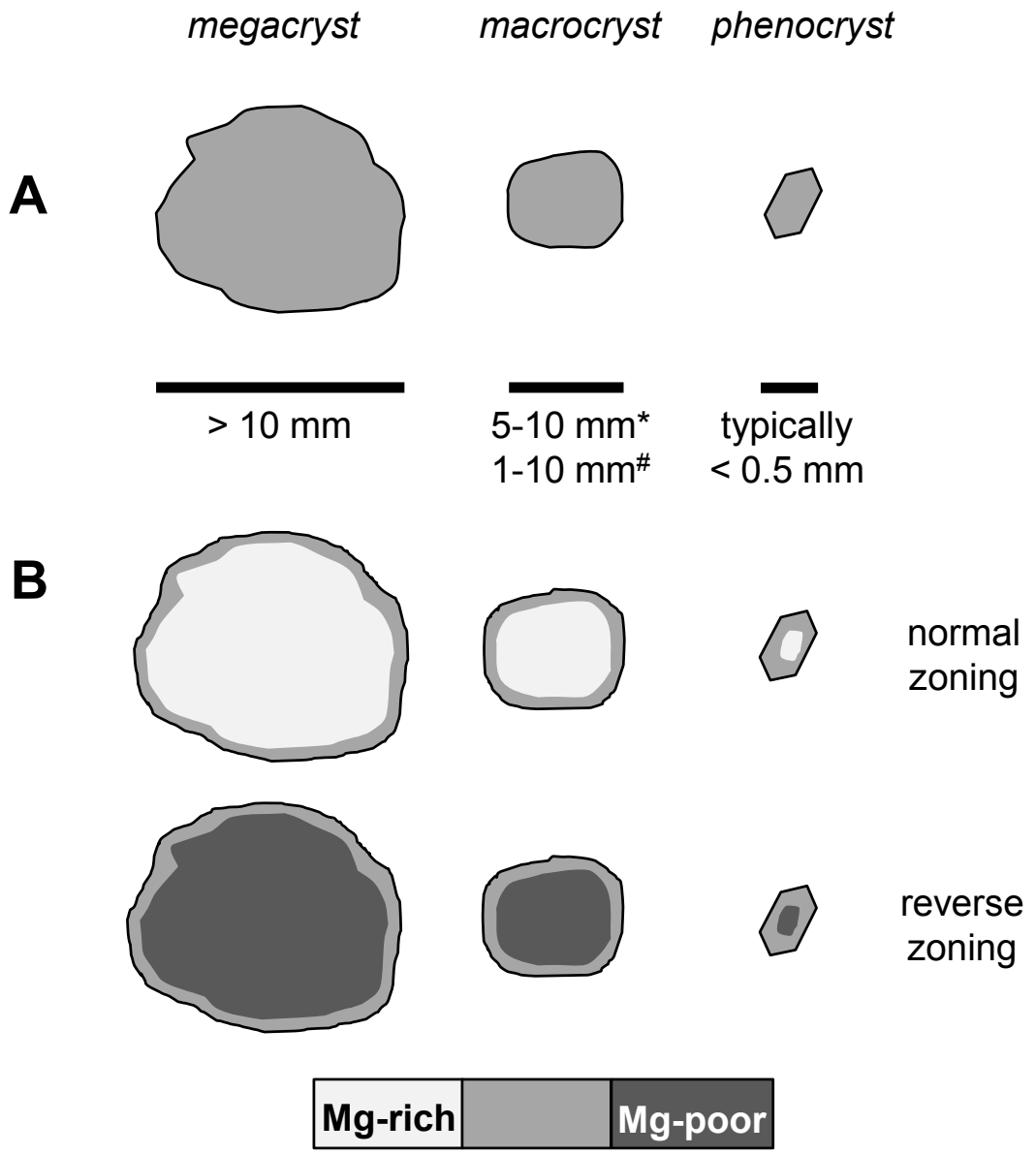

Figure 1.1: Schematics of the types and zonation relationships of kimberlitic olivines. (**A**) Morphological classification of Mitchell (2). The *asterisk* denotes Mitchell's (2) size range for macrocrysts, whereas the *pound sign* denotes that which I applied in this work. (**B**) Schematic illustrating zonation relationships of the morphological types in **A**. Olivines of all types may feature distinct overgrowth rims of nearly homogeneous Mg contents on cores of variable compositions. Composition of the core determines whether zoning is normal or reverse.

medium, which supports a kimberlitic affinity (23).

Macrocrysts (5-10 mm) are anhedral to subhedral, typically well rounded crystals of debatable origin. Earlier workers considered macrocrysts to consist of peridotite-derived xenocrysts and phenocrysts crystallized under high pressures (2, 25), but more recent works typically treat anhedral macrocrysts as xenocrysts (1, 18, 19, 26-28). On the other hand, Matveev and Stachel (11) considered crystals having NiO < 0.33 wt. % to be phenocrysts. Although the term macrocryst typically applies to crystals 5 to 10 mm in diameter, I apply it to anhedral crystals down to ~1 mm in the absence of another term.

Mitchell classified sub- and euhedral olivines as magmatic phenocrysts (1, 2). Such crystals include coarse-grained olivine (*i.e.*, macrocryst-sized) in some kimberlites, but are overwhelmingly part of the groundmass assemblage with diameters < 0.5 mm (1, 2). Other authors argued that most euhedral olivines are xenocrysts with kimberlitic rims, on the basis of compositional zoning relationships (below) (18, 19).

Megacrysts, macrocrysts, and phenocrysts have similar compositional zoning trends (18, 19, 25, 29-32) (Fig. 1.1 B). Each type commonly consists of distinct cores and rims, with either normal or reverse zoning of Mg#. Rims of each type tend to have nearly constant Mg# (typically ~88 to 90) within a given intrusion, and NiO contents ranging from > 0.35 wt. % down to ~0.1 wt. %. Cores of phenocrysts and macrocrysts have variable Mg# (~80 to ~94, typically > 85) and typically higher NiO (usually > 0.33 wt. %, with lower NiO olivines being unusually fayalitic). These zoning relationships suggest that phenocrysts and macrocrysts have the same origin (or origins) (18, 19). The core compositions of phenocrysts and macrocrysts overlap with those of megacrystic and peridotitic olivines. Thus, apart from late rims, olivine in kimberlites may consist entirely of peridotitic and megacryst-related 'xenocrysts'. (Olivines related to megacrystic peridotites may not be xenocrysts in the strict sense, because they may be genetically related to kimberlite magmas.) Therefore, whether or not H defects in kimberlitic olivine reflect conditions in kimberlite magmas throughout the ascent period depends on the extent to which the defects attain equilibrium with the magma after entrainment.

1.3 Hydrogen in Olivine

Hydrogen exists in natural olivine in trace quantities (0-600 ppm H_2O) (8), as structurally bound OH groups (*i.e.*, point defects), hydrous mineral defects/inclusions (*e.g*,

serpentine, talc), and molecular water (*e.g.*, 33-35), in order of decreasing abundance. Because H in olivine is bonded to O, I use the terms *H defect* and *OH defect* interchangeably in this thesis. Trace H is typically observed and measured using Fourier transform infrared spectroscopy (FTIR). Polychromatic infrared light is transmitted through a sample, and vibrations of chemical bonds absorb wavelengths that correspond to their vibrational frequencies. Infrared light arriving at a detector is depleted in these wavelengths, resulting in an absorption spectrum featuring peaks (also called bands) at absorbed wavelengths (*e.g.*, Fig. 1.2). Each peak corresponds to a bond in a specific crystallographic environment, or different vibrational modes of the same bond (*e.g.*, stretching, bending). Peak intensities (areas) correlate with the concentration of the absorbing bond and the sample thickness. The Beer-Lambert law (36) summarizes these relationships by relating the absorption of light (A) to the path length in the analyzed material (l), the concentration of absorbing species (C), and its intrinsic molar absorption coefficient (ε):

$$A = lC\varepsilon. \tag{1.1}$$

In the case of H defects in olivine, the intensity of wavelengths absorbed by O-H bonds correlates with the concentration of H in the crystal (37). (Hereafter, I use the conventional term *wavenumber* (inverse wavelength in cm^{-1}) instead of wavelength or frequency.)

Infrared spectra of natural olivines feature a wide variety (~70) of distinct absorption peaks (33, 34). Natural H-bearing crystals usually feature several of these bands, and the complexity of spectra varies considerably. In general, spectral complexity correlates with H content (33, 34). Infrared spectra of kimberlitic olivine are diverse, and include both simple and complex spectra (8, 11).

1.3.1 Infrared Spectra of Kimberlitic Olivine

Matveev and Stachel (11) developed a classification scheme for infrared spectra of kimberlitic olivines based on observations of hundreds of spectra, which Fedortchouk *et al*. (8) further refined (Fig. 1.2). The classification scheme also applies well to megacrystic and peridotitic (12) olivines. Spectra consist of three regions based on wavenumber: Group 1 (3420-3700 cm^{-1}), Group 2 (3260-3420 cm^{-1}), and Group 3 (3100-3260 cm^{-1}). The Group 3 region consists of a single peak of restricted abundance and I do

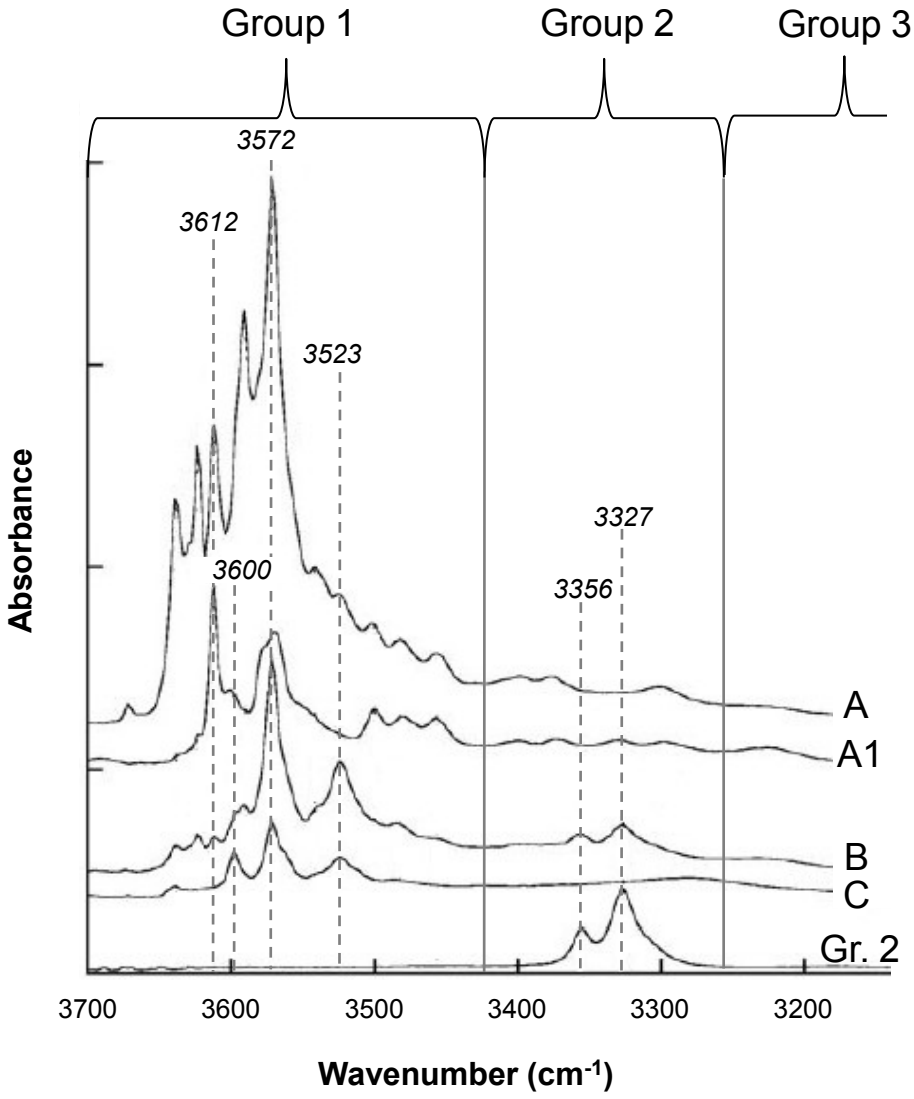

Figure 1.2: Classification of OH-related infrared spectra of kimberlitic olivine. Spectra include four main types (at right) based on the appearance of the Group 1 region. Spectra of any Group 1 type may feature two additional peaks in the Group 2 region (these peaks are present in the lower curve, and the type B spectrum). The most important peaks are indicated in by *dashed lines* and italicized wavenumbers. After Matveev and Stachel (11), and Fedortchouk *et al.* (8).

not consider it further.

The Group 1 region features a wide variety of peaks, and typically contains the greatest concentration of H of the different regions. Group 1 spectra include types A, B, and C, each of which consists of a prominent peak at 3572 cm^{-1}. Type A consists of additional peaks at higher wavenumbers (can include 3590, 3612, 3623, and 3636 cm^{-1}), and low intensity peaks at lower wavenumbers (most importantly 3500, 3523, and 3540 cm^{-1}). A peak at 3612 cm^{-1} is anomalously intense in some spectra (type A1), in which it approaches or exceeds the height of the main peak at 3572 cm^{-1}. Type C spectra are simple in comparison to type A, consisting of the main peak and two subordinate ones (3523 and ~3600 cm^{-1}), of which peak 3523 cm^{-1} is absent (or nearly so) in type A spectra. Type B spectra are intermediate between A and C; these spectra feature the fine structure of type A at wavenumbers higher than 3572 cm^{-1}, as well as the peak at 3523 cm^{-1} of type C spectra. Olivines of type A and B have the highest H contents ($\leq$ 600 and $\leq$ 500 ppm H_2O, respectively), whereas type C are relatively H-poor ($\leq$ 250, typically $\leq$ 120 ppm H_2O) (8). Type B olivines tend to be the most abundant in a given kimberlite (8, 11). Olivines of any Group 1 type may exist within a single thin section, and immediately adjacent crystals may have dissimilar spectra (11). Hydrogen contents and spectrum type do not correlate with major, minor, and trace element compositions (8, 11).

The Group 2 region comprises two peaks (3328 and 3355 cm^{-1}). These peaks can be present or absent in olivines of any Group 1 type, or may be present in the absence of Group 1 peaks. Olivines featuring Group 2 peaks do not exceed ~250 ppm H_2O (8). Group 2 peaks are typically less intense than Group 1 peaks within the same crystal. Olivines with and without Group 2 peaks can exist within a single thin section (11).

In Lac de Gras kimberlites, Group 2 bands correlate with diamond morphologies (8). Where diamonds have glossy, smooth surfaces (*i.e.*, in volcaniclastic kimberlites) similar to those produced experimentally by resorption in water (9), Group 2 bands are commonly present in olivines. In contrast, an absence of Group 2 bands characterizes olivines in hypabyssal kimberlites coexisting with corroded, rough-surfaced diamonds resembling those experimentally etched in a fluid-free environment (9). Thus, Group 2 bands may serve as a proxy for volatile saturation and diamond quality. However, the

cause of the association between Group 2-bearing olivines and water-saturated kimberlites remains unclear, if these olivines are xenocrysts.

Olivine megacrysts from the Monastery Mine (South Africa) (23) and various Siberian kimberlites (34) contain 40 to 260 ppm H_2O (normally > 100 ppm), from the few data available in the literature (23, 34). To date, spectra obtained from megacrysts include types A, A1, B, and one resembling C (but missing the peak at ~3600 cm^{-1}) (23, 34). Group 2 peaks are also present in the type C-like spectrum (34).

1.3.2 Assignment and Interpretation of OH Bands

Most, if not all, authors agree that infrared absorption bands at wavenumbers from ~3000 to ~3800 cm^{-1} in olivine result from O-H bond stretching (16, 33, 34, 38, 39). The specific nature of individual bands is more contentious. Matsyuk and Langer (34) rigorously examined polarized infrared spectra of > 300 kimberlitic and mantle-derived olivines, and surmised that of the ~70 individual types of OH identified, ~50 are intrinsic point defects. Thus, I restrict this discussion to the most prevalent peaks in kimberlitic olivines, including Group 2 peaks (because of their apparent special importance).

The main peaks in the Group 1 region may represent H occupying Si vacancies (40, 41), and H forming a coupled substitution with Ti (42). Figure 1.3 shows the most energetically favourable lattice positions of H atoms Si vacancy-related and Ti-related defects (43). The most intense peak in all Group 1 spectrum types (3572 cm^{-1}) associates with Ti in experiment, as does the second most intense peak in type C spectra (3524 cm^{-1}) (42). However, total H contents of kimberlitic olivine do not correlate with Ti concentration (11). Berry *et al*. pointed out that natural olivines with Ti-related peaks may show no correlation between H and Ti, because both elements are incorporated into olivine by multiple mechanisms, some of which do not involve the other. For example, Ti occupies both tetrahedral sites (Si vacancies, no association with H) and octahedral sites (forming a hydrous Ti-clinohumite-like defect), such that Ti concentration in olivine can exceed H concentration (42). Conversely, H is incorporated into olivine via both Ti-related and Ti-unrelated sites (such as Group 2 and other Group 1 defects) (40, 41, 44), thereby allowing H concentrations to exceed Ti concentrations. Thus, the absence of correlations between Ti and H in kimberlitic olivine does not discount the presence of Ti-related H defects.

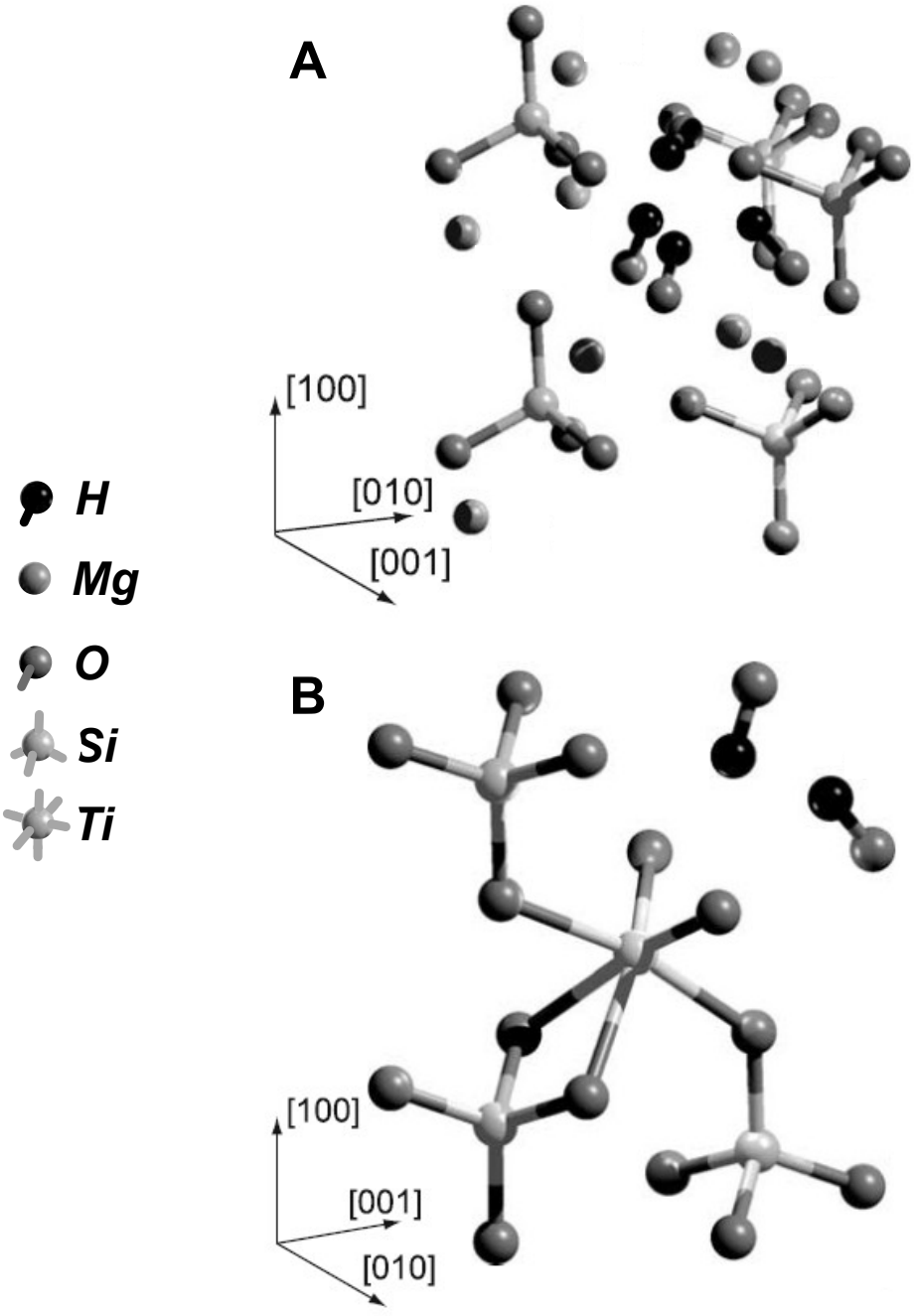

Figure 1.3: Models of the positions of H defects associated with Si vacancies and octahedrally coordinated Ti defects. (**A**) Hydrogen positions associated with Si vacancies. (**B**) Hydrogen positions associated with octahedrally coordinated Ti. After Walker *et al*. (43).

The identity of the other Group 1 peaks is less clear. In experiment, Group 1 peaks generally intensify with decreasing silica activity (40, 41), suggesting that these peaks represent H in Si vacancies. However, these experiments did not reproduce all of the peaks that typify Group 1 A and B spectra. Matveev and Stachel (11) proposed that the structure of peaks in this region is a function of pressure, based on comparison with spectra from low pressure (45, 46) and high pressure experiments (15, 40, 47); indeed, the triplet peaks from 3456-3500 cm^{-1} (type A1, Fig. 1.2) appear only in the run products of experiments above 2 GPa. However, their interpretation that type C spectra represent equilibrium pressures < 1 GPa is not consistent with the production of these spectra in Ti-doped experiments at 1.5 GPa (42), nor their presence in olivines from spinel facies (48) and diamond-bearing peridotites (12). Thus, Group 1 peaks (other than those associated with Ti) may represent H associated with Si vacancies, but their structure is unlikely to constitute a reliable geobarometer.

Group 2-bearing olivines form in experiments buffered under oxidizing conditions (typically at or near the Ni-NiO buffer) (40, 42, 44, 46, 49), and in experiments doped with trivalent cations (44). Thus, Group 2 peaks probably represent H forming a coupled substitution with trivalent cations (including Fe^{3+} in oxidizing experiments). However, these peaks typically do not form in experiments with silica activities below that of the olivine-orthopyroxene buffer. Matveev and Stachel (11) suggested that Group 2 peaks require both high silica activity and trivalent cation impurities. This interpretation provides the best reconciliation between apparently contradictory experimental results.

Matveev and Stachel (11) interpreted Group 2-bearing olivines in kimberlites as xenocrysts equilibrated under orthopyroxene-buffered (*i.e.*, high silica activity) conditions in peridotites (11). In contrast, Fedortchouk *et al*. (8) suggested that Group 2-bearing olivines re-equilibrated with exsolved kimberlitic fluid during emplacement. The presence of Group 2-bearing olivine in peridotite xenoliths (12, 33, 34, 50), coupled with the requirement of coexisting orthopyroxene, supports the interpretation that these olivines are lherzolitic or harzburgitic xenocrysts. The interpretation that Group 2 H incorporates into olivine during equilibration with kimberlitic fluid developed from the exclusive association of Group 2-bearing olivines with volcaniclastic kimberlites (within

Lac de Gras kimberlites), which contain diamonds apparently resorbed by magmatic water (8). In keeping with this idea, Berry *et al*. (44) speculated that in peridotitic olivines, these defects form subsequent to primary hydrogenation during oxidation, probably concomitant with exhumation (*i.e.*, magma and xenolith ascent). However, if this argument holds, the prevalence of Group 2-bearing olivines should correlate with the oxidation state of the host magma; no such correlation exists among the Lac de Gras kimberlites, among which the most and least oxidizing magmas (51) both contain abundant Group 2-bearing olivines (8). Thus, Group 2-bearing olivines may well be xenocrysts that have not equilibrated with kimberlite magma. However, this interpretation does not explain the distribution of Group 2-bearing olivines in Lac de Gras kimberlites; I hypothesize that these crystals associate with volatile-saturated kimberlites because the faster ascent rates of these magmas permit better preservation of mantle-derived spectra.

1.3.3 Modification of H Defects during Kimberlite Magmatism

Miller *et al*. (33) pointed out that olivine equilibrated at high pressure transported to Earth's surface in magmas may either lose (water-poor magmas) or gain (water-rich magmas) H by diffusive exchange with its new environment. Indeed, subsequent experiments (13, 14) showed that H-diffusion in olivine is sufficiently rapid to allow significant changes in H-content during magma ascent. Experimental determinations of the H-solubility in olivine (13, 15, 16) show that increasing pressure produces greater solubility, probably as a consequence of concomitant increases in the fugacities of H_2 and H_2O. Because ascending crystals in nature likely experience decreasing fugacities of H_2 and H_2O related to decompression, even in a pure aqueous fluid, crystals that attained equilibrium at depth may well lose H during ascent (13, 14). Unless these processes result in complete re-equilibration, they should produce zonation of H in the partially dehydrated olivines.

Most kimberlite-hosted xenolith olivines show little to no zonation of H (17, 52, 53), whereas some have H-poor rims (Finsch kimberlite, South Africa) (52). The extent to which this zonation reflects re-equilibration with kimberlite magma remains unclear, because the authors of these studies specifically analyzed crystals away from the margins of the xenoliths, where interaction with magma may be inefficient. Assuming that the H

zonation reflects olivine-magma interactions, its variability among different localities and samples indicates that magmatic resetting of H defects may depend on the ascent dynamics of specific xenoliths, the activity of water in the host magma, and/or contrasting behaviour of different H defect types. Whatever the exact reason for the variability, zonation of H in free olivine crystals (xenocryst or phenocrysts) could also vary among different intrusions and individual crystals. Whether zonation of Group 2 defects in kimberlite-hosted olivines differs from that of Group 1 defects remains unclear.

Other studies tested homogeneity of H in olivine megacrysts and those of unspecified morphology (23, 54), although the data are few and the authors provide no specific details regarding the choice of analysis locations. Bell *et al*. (23) reported that megacrysts from the Monastery Mine (South Africa) are typically homogeneous within the uncertainties of their analyses, and on the scale of their infrared beam. However, the authors were not fully convinced that the H contents of their olivines were completely unmodified. Olivines (macrocrysts or megacrysts?) from the Udachnaya kimberlite show limited variation in H contents and relative peak intensities at the 5 μm scale, in crystals lacking an optically visible hydrous mineral exsolution texture (54). Though limited in number, existing data suggest that heterogeneity of H in kimberlitic olivines is usually minimal, which may indicate restricted modification of H contents during ascent.

Fedortchouk *et al*. (8) reasoned that olivine in kimberlite, including xenocrysts, has probably equilibrated with water-rich kimberlite magma/fluids. They cite the lower H contents of xenolith olivines of Peslier *et al.* (17) (0-80 ppm H_2O) compared to those in their kimberlitic samples (commonly > 100 ppm H_2O) as evidence of hydrogenation of xenocrysts during transport in kimberlite magma. Indeed, although xenolith olivines with up to ~270 ppm H_2O exist (34), none reported to date reaches a concentration as high as the kimberlitic upper limit of 600 ppm H_2O (8); most xenolith olivines contain < 150 ppm H_2O. However, if we include olivine megacrysts as a type of xenocryst, and some macrocryst-sized olivines have a megacrystic affinity (as supported by overlapping compositions (2)), the discrepancy between H contents of kimberlitic and xenolith olivines is significantly less; megacrysts routinely have H_2O > 150 ppm (23, 34), although no data show megacrysts having above 260 ppm H_2O. Thus, H contents of kimberlitic olivines may or may not support magmatic re-equilibration of xenocrysts. I

believe the diversity of spectra among kimberlitic olivines, and the complete overlap of spectrum types between these and xenolith olivines, could indicate that most xenocrysts have not approached equilibrium with their host magmas, with respect to H. In this regard, H defects in kimberlitic olivine may reflect magmatic processes only insofar as the extent of diffusive re-equilibration permits. Thus, the use of H defects in these olivines as proxies for magmatic processes and diamond potential requires elucidation of the degree to which H defects of xenocrysts re-equilibrate.

1.4 This Study

1.4.1 Statement of Problem and Objectives

The above sections illustrate that, if kimberlitic olivines are predominantly xenocrysts, we must understand the degree to which H exchanges between these xenocrysts and kimberlite magma to make meaningful interpretations of H defects. The apparent absence of H zonation in kimberlitic olivine (23, 54) suggests ineffective H exchange. However, if the majority of coarse-grained olivines in kimberlites are xenocrysts, the olivines from the adjacent Lac de Gras kimberlites should exhibit no variation in the abundance of Group 2 peaks or H concentrations, assuming lateral homogeneity of the mantle beneath the Lac de Gras region. Thus, the preferential distribution of Group 2-bearing olivines in volcaniclastic kimberlites (8) suggests some magmatic overprint on H defects of olivine xenocrysts. The objectives of this study focus on elucidating the extent to which H in xenolith-derived olivines re-equilibrates with kimberlite magmas, to better delineate whether these defects can be employed as proxies for magmatic water activity and diamond potential.

Objective 1

To elucidate whether zonation of H defects in xenolith olivines in contact with kimberlite magma involves introduction or attenuation of Group 2 defects, and relative increases or decreases in H content. I hypothesize that crystals in contact with surrounding kimberlite will exhibit different zonation from those that are better protected in the cores of xenoliths, and that this zonation will result in a distinctive kimberlitic spectrum type. I also hypothesize that Group 2 peaks will attenuate in the rims of crystals.

Objective 2

To compare H defect-zonation in (predominantly xenocrystic) macrocrysts with that in

xenolith olivines to elucidate whether xenocrysts better re-equilibrate with kimberlite magmas than olivines enclosed within xenoliths. I hypothesize that macrocrysts will exhibit similar H zonation trends to xenolith olivines in contact with kimberlite, including attenuation of Group 2 peaks in the rims.

1.4.2 Scope

This study examines zonation of H-related infrared spectra of olivine in peridotite xenoliths and/or olivine macrocrysts from four kimberlites: Jericho (Nunavut, Canada) and Beartooth (Lac de Gras, NT, Canada), and Matsoku and Pipe 200 (Lesotho). The project focuses on FTIR spectroscopy of these olivines, and includes petrography and electron microprobe analysis. I coupled the FTIR spectroscopy analyses to the petrographic context of the xenolith olivines, to elucidate whether crystals in contact with kimberlite preserve a distinct zonation record by comparison to crystals in the centres of xenoliths. I do not relate the findings to the specific geological context of the samples (*i.e.*, kimberlite lithofacies), as these details are not available for most samples. Although I include simple H diffusion models to help explain the findings, I do not attempt to estimate ascent durations on the basis of these models, as previous workers have (17, 50, 55); I believe the uncertainties regarding the activity of water in kimberlite magmas and the depth of its exsolution impose severe limitations on such attempts. I relate the H zoning trends to the relative diamond grades (*i.e.*, concentrations) of the barren (Matsoku, Pipe 200) and diamondiferous (Jericho, Beartooth) host kimberlites, to assess whether H zonation may be a useful proxy for diamonds for new kimberlite discoveries.

1.4.3 Claim

In keeping with previous works, this study shows that zonation of H in xenolith olivines varies among samples and localities. Where significant zoning exists, H concentrations decrease in the rims. Crystals adjacent to kimberlite feature the same zonation as those in the cores of xenoliths. Among olivine macrocrysts, zonation of H is also variable, but typically involves relative depletion of H in rims. Thus, little evidence exists for diffusive hydrogenation of olivines during transport, although such trends could be overprinted by later loss of H. Macrocrysts and xenoliths from the same kimberlites appear to have similar zonation trends, indicating that both types of olivine experience similar degrees of modification in a given intrusion. If previous interpretations of weak H zonation patterns

(17, 50, 55) are correct, this finding may indicate that olivine xenocrysts generally do not equilibrate effectively with kimberlite magmas, with respect to H.

Comparison of measured H-zonation with simple models of H diffusion in olivine shows that weakly zoned olivines must have ascended rapidly through the lithosphere at elevated water activities. The more strongly zoned crystals could have experienced slower ascent rates, resided in more water-poor magma, or experienced higher temperatures than the weakly zoned crystals. A combination of these factors could also explain the differential zonation.

The degree of H-zonation in xenolith and macrocrystic olivines appears to reflect the diamond grade of the host kimberlite; the barren kimberlites Matsoku and Pipe 200 contain strongly zoned crystals, whereas olivines from the diamondiferous Jericho and Beartooth kimberlites feature weaker zoning. However, future studies must confirm these findings in a more comprehensive dataset before H-zonation can be reliably applied as a proxy for diamond.

In the Beartooth kimberlite, zoned olivines typically feature stronger zoning of Group 2 defects than Group 1 defects; Group 2 defects more strongly attenuate in the rims. This finding suggests these defects diffuse out of olivine more readily following immersion in kimberlite magma than do Group 1 defects. Preferential loss of Group 2 H may explain the exclusive association of these olivines in water-saturated kimberlites of the Lac de Gras kimberlites; water-saturated magmas may ascend sufficient rapidly to preserve these peaks, whereas in water-undersaturated magmas, these defects may completely diffuse out of olivine during a longer transport period.

1.4.4 Agenda

In the next chapter, I describe the details of sample preparation, electron microprobe analysis, and FTIR spectroscopic analysis and data processing. In Chapter 3, I describe my findings, which bear mainly on the zonation of H in the examined olivines, and how this phenomenon varies among my samples. This section also includes petrographic descriptions and the compositions of olivine. In Chapter 4, I employ simple models of H diffusion in olivine to explore the parameters that could explain the variations among different localities, and how variations in these parameters may also influence the preservation of diamond during transport in kimberlite magmas. Finally, I provide

suggestions of additional work that could further test many of the hypotheses that arose during the course of this investigation.

CHAPTER 2

MATERIALS AND METHODS

2.1 Sample Selection and Preparation

2.1.1 Xenoliths and *In Situ* Macrocrysts

Peridotites examined in this study were chosen from fifteen xenoliths from southern African kimberlites and the Jericho kimberlite (Nunavut, Canada) (Fig. 2.1), on the bases of the degree of alteration and clarity of olivine. Drs. Maya Kopylova and Barrie Clarke donated the samples from Jericho and southern Africa, respectively. Doubly polished sections were produced from hand samples such that their original locations within the xenolith were preserved (Fig. 2.2). Slabs (~0.5-2 cm thick) were cut through the centres of the xenoliths along their short axes. Section locations were marked on the slabs, and each was photographed. One to three doubly polished sections (~300-400 μm thick), fastened to glass slides with acetone-soluble adhesive, were produced from each sample at the Thin Section Preparation Laboratory (Department of Earth Sciences, Dalhousie University). The sections were examined with a Nikon Eclipse LV100 petrographic microscope to assess the degree of alteration and deformation of olivine. From these samples, four xenoliths with mainly undeformed, unaltered olivine were chosen for FTIR and electron microprobe analysis: two from Jericho (samples LGS-011 and -53), one from Matsoku, Lesotho (sample 26/10), and one from Pipe 200, Lesotho (sample 26/32); one or two normal thin sections were made from each of these samples for petrographic observation. Polished sections of three of these samples contained some kimberlite attached to the xenoliths (both Jericho samples and the Pipe 200 xenolith). In these sections, olivine macrocrysts were analyzed in addition to xenolith olivines.

The sections were photographed at 20X magnification using a Nikon DS-Fi1 camera and an Olympus SZ61 binocular microscope, and scanned for record-keeping purposes during FTIR analysis. The sections were then immersed in acetone in an ultrasonic cleaner for a period of ~1-8 hours to liberate the sections from their glass slides. The sections remained intact following dissolution in acetone. The FTIR analyses were performed on the liberated sections.

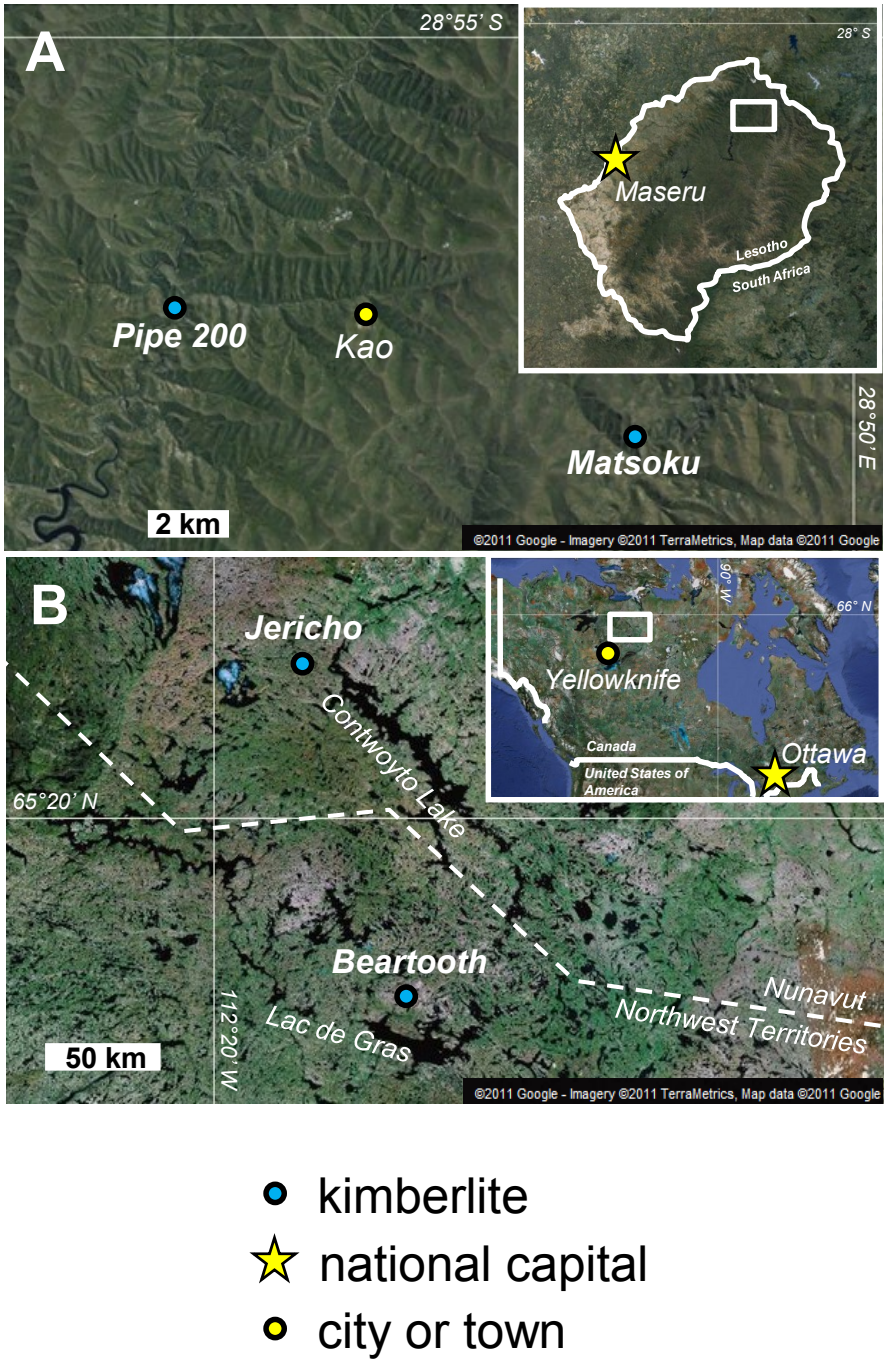

Figure 2.1: Satellite images illustrating the locations of kimberlites investigated in this study. (**A**) Locations of the Matsoku and Pipe 200 kimberlites. Inset shows the position of the magnified view. (**B**) Locations of the Jericho and Beartooth kimberlites. Inset shows the position of the magnified view. All images were obtained from Google Maps ©.

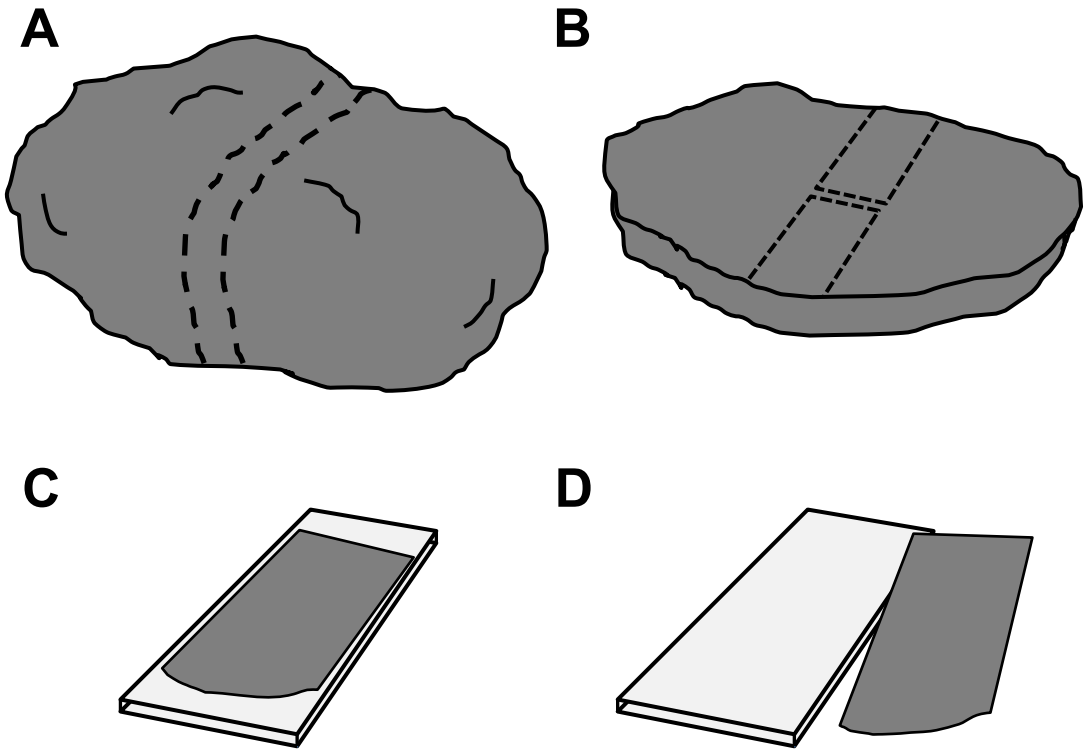

Figure 2.2: Section preparation method. (**A**) Slabs were cut through the centres of the xenoliths along their short axes. (**B**) Slabs were marked and photographed prior to sectioning. (**C**) Glass-mounted, doubly polished sections were then observed, analyzed using the electron microprobe, and photographed. (**D**) Sections were liberated from the glass slides following immersion in acetone prior to FTIR analysis These procedures allowed analytical results to be interpreted in terms of distance from adjacent kimberlite.

2.1.2 Macrocrysts from Mineral Separates

Olivine macrocrysts from the Beartooth kimberlite (NT, Canada) were manually selected from a heavy mineral separate, provided by BHP Billiton Diamonds, Inc. Grains were chosen on the basis of optical clarity and low degrees of alteration. Selected grains are mainly rounded or fragmental anhedral crystals, with some essentially euhedral tabular crystals, and range from ~1-2 mm in diameter. The grains were placed onto packing tape inside ~25 mm diameter plastic rings, and the rings were filled with epoxy. The epoxy mount was ground down until all grains were exposed, and then hand-polished using polishing paper (with or without a polishing wheel) with diamond pastes and suspensions down to < 1 μm particle size. The polished face was then glued to a glass slide. The unpolished side was sawn off using a Buehler IsoMet low speed saw, such that ~100 to ~400 μm of the mount remained attached to the glass slide. The newly sawn side was then polished using the procedure outlined above. The mount was then left in acetone to soften the epoxy, and the grains were removed using tweezers. These procedures produced olivine platelets with their upper and lower surfaces ground away, leaving the interiors of the crystals exposed. The FTIR measurements were performed on the liberated grains (see below). Selected grains were remounted in epoxy and re-polished for electron microprobe analysis.

2.1.3 Characteristics of the Host Kimberlites

Previous works describe to varying degrees the geology and petrography of the kimberlites studied here (8, 56-58). The kimberlites differ in terms of the complexity of their emplacement; Jericho (58) and Pipe 200 (56) contain several phases of magma that have distinct textural characteristics, including both magmatic and volcaniclastic type kimberlitre. On the other hand, Beartooth (8) and Matsoku (57) are less complex. The kimberlites also differ in terms of relative diamond grades; Jericho (*e.g.*, 59) and Beartooth (*e.g.*, 8) are both diamondiferous, whereas Matosku is barren (J. Gurney, pers. comm., 2011) as are two of three phases of Pipe 200 (56). Otherwise, insufficient details are available (except for Jericho) to compare and contrast the emplacement histories or mineralogical characteristics of these kimberlites.

2.2 Electron Microprobe Analysis

Electron microprobe analysis was undertaken to characterize the chemical composition of the xenolith and macrocryst olivines. Samples were observed in backscattered electron mode to visualize chemical zonation patterns prior to analysis. Major (Mg, Fe, Si), minor (Mn, Ni) and trace (Al, Ca, Cr, Cu, Na, P, Ti, Zn) element analyses were performed using a JEOL 8200 electron microprobe in the Department of Earth Sciences, Dalhousie University. Analytical conditions, standards, and detector crystals are listed in Table 2.1. An olivine standard was run about every ten analyses to control for intrumental drift. When control analyses yielded totals < ~99 %, only those analyses performed prior to and after correct control analyses (total > 99%, wt. % oxides within accepted uncertainties) were accepted. Standard ZAF corrections were applied to the raw data.

Sections were observed in backscattered electron mode to identify compositional zones. Where zoning was not apparent, a minimum of five grains was analyzed from each xenolith to test for compositional heterogeneities undetectable in backscattered electron images.

Table 2.1: Details of electron microprobe analysis protocol.

	Detector		**Count Time (s)**		**Accelerating**	**Probe**
Element	**Crystal**	**Standard**	*Peak*	*Background*	**Voltage (kV)**	**Current (nA)**
Si	TAP	Olivine	20	10	20	100
Ti	PETJ	Kaersutite	100	40	20	100
Al	TAP	Sanidine	100	40	20	100
Cr	PETJ	Cr metal *or* chromite	100	40	20	100
Fe	LIFH	Olivine	20	10	20	100
Mn	LIFH	Pyrolusite	40	20	20	100
Cu	LIFH	Chalcopyrite	100	40	20	100
Zn	LIFH	Sphalerite	100	40	20	100
Ni	LIFH	Ni metal	40	20	20	100
Mg	TAPH	Olivine	20	10	20	100
Ca	PETJ	Kaersutite	100	40	20	100
Na	TAPH	Jadeite	100	40	20	100
P	PETJ	Fluoroapatite	100	40	20	100

Macrocrysts in thin section (Jericho) were analyzed once or twice (one analysis for each compositional zone analyzed). The Beartooth olivines in grain mount were analyzed at least twice (usually three or more times). These manually polished mounts tended to give lower totals than desired (some < 99%); the greater number of analyses was performed to check for consistency between analyses. No microprobe analyses were performed on Pipe 200 macrocrysts.

2.3 Fourier Transform Infrared Spectroscopy

2.3.1 Data Collection

Unpolarized infrared spectra of olivine were obtained over the wavenumber range 650-4000 cm^{-1} or 650-5500 cm^{-1} (Beartooth macrocrysts only) in transmitted light mode, using a Thermo-Nicolet Nexus spectrometer and Continuum infrared microscope (De Beers Laboratory of Diamond Research, University of Alberta). These wavenumbers include the regions corresponding to OH-related absorptions (3000-3700 cm^{-1}), as well as Si-O overtone peaks (1500-2100 cm^{-1}). The stage was flushed with dried air throughout the analyses to minimize interference from water vapour in the laboratory air. The spectra were compiled from 200 scans at 4 cm^{-1} resolution. Analyses were performed using a square light beam 50x50 μm^2, or 100x100 μm^2 (Beartooth macrocrysts only) in cross section.

Multiple spectra were collected along profiles through individual crystals to assess zonation trends. Profiles of five or more points were collected from olivines in each xenolith, and were supplemented with profiles of fewer points and core-rim pairs to verify that the trends were consistent throughout the xenolith. Grains were analyzed both at the margins and within the cores of xenoliths.

Core and rim analyses were performed on most macrocrysts. Some small or highly fractured crystals could be analyzed in the core or rim alone. Analysis locations as close as possible to the grain boundary were chosen as ‘rim’ locations; in the case of macrocrysts from Beartooth, rim analyses were performed on regions that appeared to represent primary grain boundaries, as opposed to fractured surfaces that may be relics of separation processing. Multiple-point profiles were measured along some of the larger macrocrysts from Jericho and Pipe 200.

2.3.2 Processing of Infrared Spectra

Infrared spectra were classified according to the scheme illustrated in Figure 1.2. Spectra obtained from different locations within individual crystals were compared visually to qualitatively assess changes in peak intensity and spectrum type. Integrated absorbance intensities (*i.e.*, peak areas, A_{int}) were calculated using an automated macro (modified after Matveev and Stachel (11)), run using Omnic© and Macros Basic© software. Use of the macro enabled rapid processing of > 400 spectra. The macro integrates peak intensities for Group 1 and Group 2 peaks over the respective ranges 3653-3415 cm^{-1} and 3415-3264 cm^{-1}, using a separate linear baseline for each group of peaks. The baselines were defined by the intensity values at 3653 and 3415 cm^{-1} (Group 1), and 3415 and 3264 cm^{-1} (Group 2); absorption peaks rarely overlap with these locations. This method of baseline selection differs from that of the original macro (11), wherein a linear baseline defined at 3755 and 3130 cm^{-1} was applied to all OH-related peaks. The procedure was modified because different spectra from the same crystals yielded A_{int} values that did not always correlate with qualitative intensity changes observed during visual comparison of spectra, apparently as a consequence of differing (in some cases, subtly) baselines. Selecting baselines closer to the actual peaks prevented such discrepancies. In some cases, particularly where the tail of a broad, asymmetric peak at ~3690 cm^{-1} produced nonlinear baselines, baselines were manually fitted prior to processing with the macro. This peak has the same wavenumber as serpentine inclusions (33-35, 54), but varies in intensity as the beam focus is adjusted (S. Matveev, pers. comm., 2011), in contrast to proper H defect peaks, which remain constant. The peak intensifies near fractures, grain boundaries and inclusion arrays, where serpentine is common. Thus, in these samples, this peak appears to represent serpentine external to the olivine, which variably interacts with the infrared beam as the focal position and beam position are adjusted.

Kovacs *et al*. (60) showed that the type of H defect strongly influences the molar absorption coefficient of OH bonds in olivine; Ti-related OH bonds absorb about three times less infrared light than Si vacancy-related OH bonds, despite the similar wavenumbers of their infrared peaks. If these findings are correct, widely accepted methods employing wavenumber-dependent absorption coefficients (37, 61) are unreliable. Consequently, Kovacs *et al.* (60) suggest that quantitative determination of H

concentration in nominally anhydrous minerals requires that the types of H defect responsible for the absorption peaks, as well as their specific absorption coefficients, be known. Because of these problems, and because absolute H concentration is not important for the objectives of this study, quantitative estimates of H concentration are not provided.

2.3.3 Uncertainties of Integrated Absorbance Intensities

Uncertainties of calculated A_{int} derive from the method of baseline selection and spectral noise. Spectra collected in this study using a 50x50 μm^2 beam were sufficiently noisy (Figure 2.3 shows an extreme example) that resulting uncertainties required evaluation, particularly for low-intensity spectra. Upper and lower A_{int} limits were calculated using baselines fitted to the lowest troughs and highest peaks of background noise, respectively (Fig. 2.3). Half of the difference between the upper and lower A_{int} was considered to represent the maximum uncertainty resulting from spectral noise. Repetition of this procedure on several spectra yielded approximate (*i.e.*, average) noise-related uncertainties of ± 0.25 cm^{-1} (Group 1, 50x50 μm^2 beam), ± 0.06 cm^{-1} (Group 1, 100x100 μm^2 beam), and ± 0.009 cm^{-1} (Group 2, 100x100 μm^2 beam). Although any given spectrum might have a different uncertainty than the average, this approach provides a reasonable alternative to repeating the procedure on > 400 individual spectra.

Uncertainties related to baseline selection are difficult to quantify because manual baseline fitting is a subjective procedure. Peslier and Luhr (55) estimated these uncertainties by carrying out repeated manual baseline fits, and observing the scatter in the resulting A_{int} values. They estimated uncertainties on the order of ± 0.2 cm^{-1}. Although this procedure was not performed on the data presented here, uncertainties on this order to apply. However, because spectra from the same crystal usually have similar baselines, and the same baseline fitting method was applied, uncertainties resulting from different baseline fits may contribute little to relative error within a given crystal. That is, these errors should be systematic if the baselines are defined at the same coordinates and the spectra are similar. As zoning of spectra within individual crystals is the main phenomenon of interest here, the reported uncertainty estimates are based on spectral noise alone.

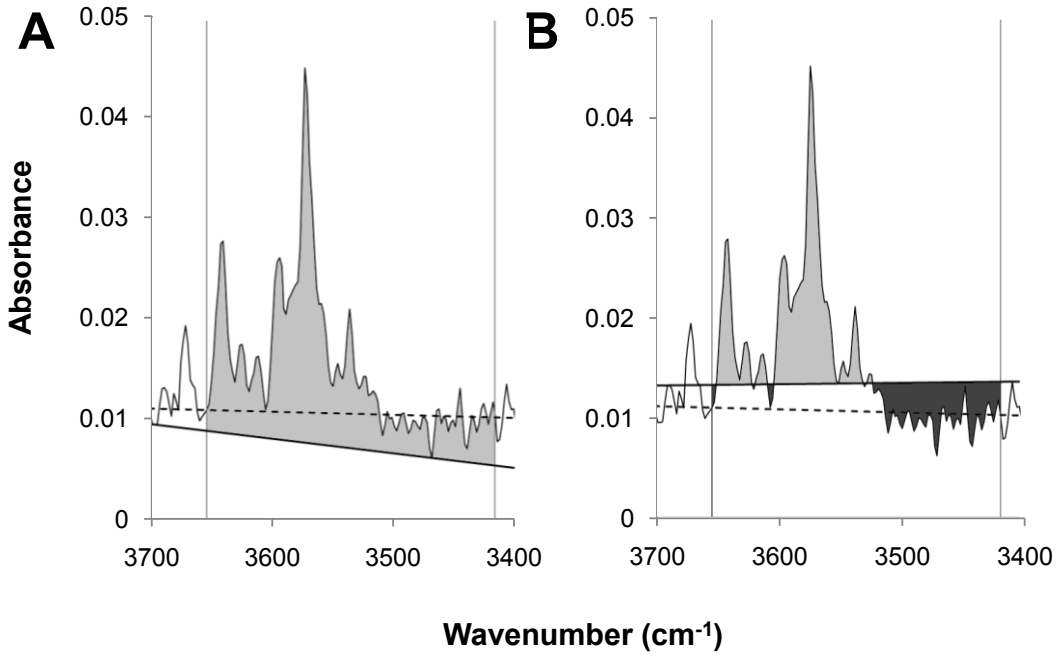

Figure 2.3: Method of estimating uncertainty of integrated absorption intensities. Uncertainty was estimated as half the difference between integrated intensities calculated from lower (**A**) and upper (**B**) baseline fits. The chosen lower and upper baselines are fitted through the troughs and peaks of the background noise, respectively. The integrated absorbance intensity is the sum of the areas above (*i.e.*, positive, *light grey areas*) and below (*i.e.*, negative, *dark grey areas*) the baseline. This spectrum was chosen for this figure because its unusually noisy background clearly illustrates the effect of baseline choice. *Vertical lines* bracket the region of the spectrum integrated for Group 1 peaks. The *dashed line* is the baseline used by the macro, as defined at the intersection of the spectrum with the two vertical lines.

CHAPTER 3

RESULTS

3.1 Petrography

3.1.1 Jericho Xenoliths and Kimberlite

The two garnet harzburgite xenoliths from the Jericho kimberlite (Fig. 3.1) consist predominantly of olivine and orthopyroxene, with minor garnet and an opaque Cr-spinel, and accessory diopside. The olivines range in average diameter from ~0.6 to 2.2 mm (sample 011; average = 1.5 mm) and 0.9-4.1 mm (sample 53; average = 2 mm). At least two generations of secondary minerals are present. The first includes relatively fine-grained, high surface area intergrowths of phlogopite and spinel (identified by optical microscopy) in contact with garnet (Fig. 3.1 C), and diopside with or without amphibole in contact with orthopyroxene (Fig. 3.1 D). Backscattered electron images show bright rims (≤ 100 μm) on olivines in apparent association with the first generation of secondary minerals. The distribution and thickness of the first generation of secondary mineral growths do not obviously vary with distance from the margin of the xenolith (*i.e.*, nearness to kimberlite). Later secondary minerals include fine-grained serpentine group minerals and associated accessories along grain boundaries, cleavages, and fractures (Fig. 3.1 A, B, D). The late alteration crosscuts the bright olivine rims, and in some cases veinlets cut through the interior of olivine (Fig. 3.1 D). Chlorite replaces orthopyroxene where alteration is spatially restricted. A wide variety of accessory minerals is associated with the late alteration assemblage; a detailed description of these minerals and their textures is beyond the scope of this work.

Sample 011 is less altered than sample 53; in the former, the later secondary minerals mainly exist in narrow zones along grain boundaries, whereas pseudomorphs of secondary minerals almost completely replace some crystals in sample 53. Despite this significant replacement, many crystals appear to preserve their original grain boundaries. Orthopyroxene is more severely altered than olivine in this sample, where in many cases only vestiges of it remain in cores of unidentifiable, opaque replacement products.

The Jericho kimberlite attached to sample 53 consists of dark, greenish lapilli of hypabyssal kimberlite coating the xenolith, enclosed by lighter grey volcaniclastic

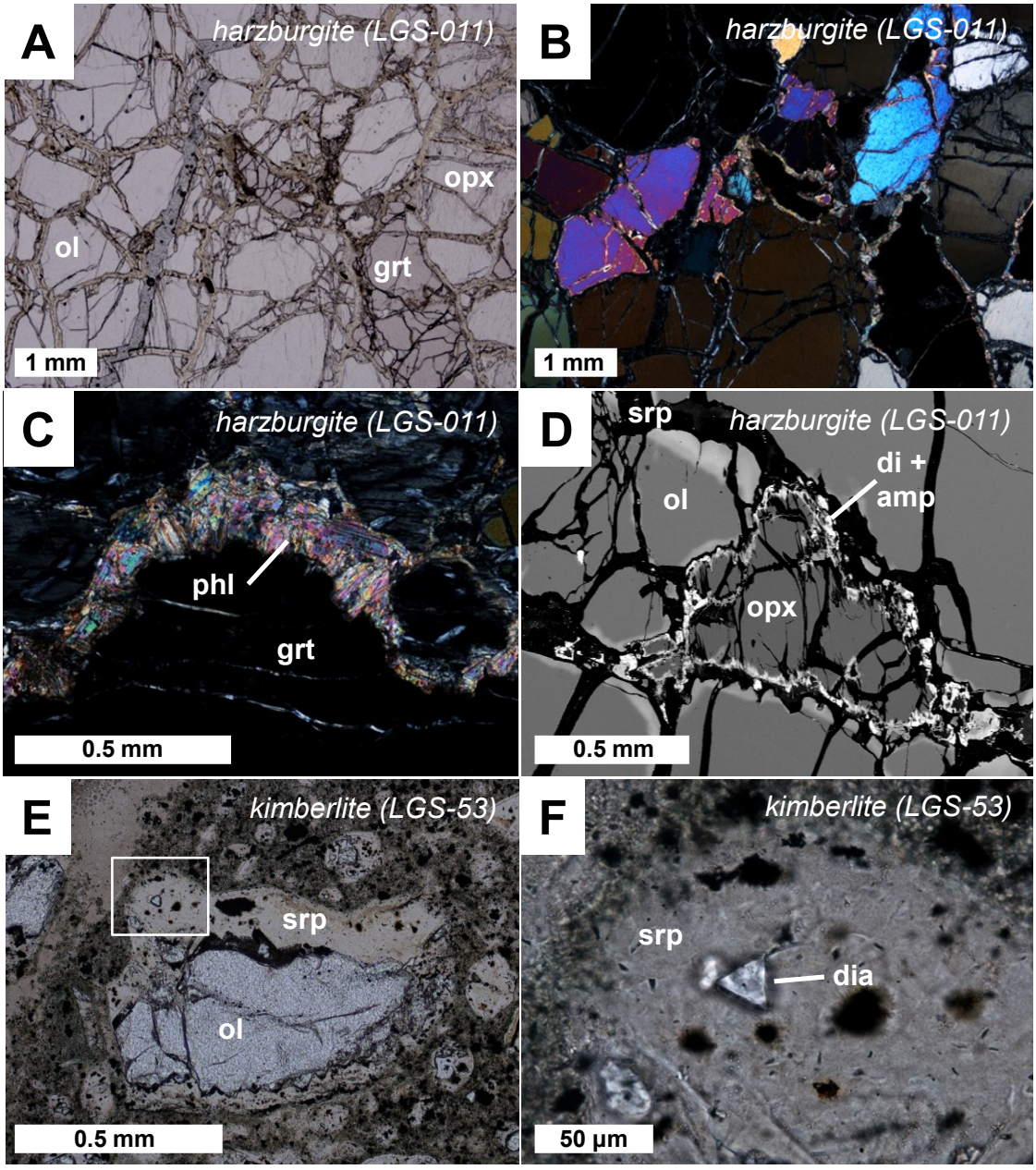

Figure 3.1: Characteristics of the Jericho xenoliths and kimberlite. **(A, B)** Coarse-grained, anhedral olivine and orthopyroxene partially replaced by serpentine (pale yellow in **A**). **(C)** Phlogopite rims on garnet. **(D)** Partial replacement of orthopyroxene by diopside ± amphibole and bright rims of olivine on primary olivine. (**E**) Serpentine partially replacing an anhedral olivine macrocryst in kimberlite. Box shows location of **F**. (**F**) Diamond inclusion in serpentine pseudomorph after olivine. (**A**, **E**, and **F**) Plane-polarized light photographs. (**B**, **C**) Crossed polarized light photographs. (**D**) Backscattered electron image. ***amp*** – amphibole, ***di*** – diopside, ***dia*** – diamond, ***grt*** – garnet, ***ol*** – olivine, ***opx*** – orthopyroxene, ***phl*** – phlogopite, ***srp*** – serpentine.

kimberlite. Both types of kimberlite contain a matrix of (mostly) isotropic, homogeneous, orange-yellow serpentine with fine-grained carbonates, surrounding larger crystals. In the lapilli coating, larger crystals are mainly sub- and euhedral olivine smaller than 1 mm in diameter. Some of these olivines contain inclusions of rutile throughout, and one partially pseudomorphed, anhedral olivine (Fig. 3.1 E) contains an inclusion of euhedral diamond (~20 μm in diameter) in the serpentine pseudomorph (Fig. 3.1 F). Fine opaque minerals (chromite? magnetite?) are abundant in the groundmass. Larger (> 1 mm) macrocrysts of sub- and anhedral olivine predominate in the enclosing kimberlite. This kimberlite also contains garnet and phlogopite macrocrysts, and crustal xenoliths of limestone and/or marble.

3.1.2 Matsoku Xenolith

The garnet lherzolite xenolith from Matsoku (Fig. 3.2) consists predominantly of olivine and orthopyroxene with minor garnet and diopside, and accessory phlogopite. Olivine ranges in average diameter from ~0.6 to 1.9 mm, and is usually finer-grained than orthopyroxene and garnet (Fig. 3.2). Most clinopyroxene and phlogopite concentrate around garnets; both range from having low surface area contacts to irregular, interlocking grain boundaries; some have interstitial textures with respect to orthopyroxene and olivine (Fig. 3.2 A). The diopside and phlogopite are coarse-grained relative to secondary phlogopite and diopside from the Jericho xenoliths. Garnet has anhedral, variably embayed margins filled with adjacent diopside or phlogopite. Secondary minerals consist of serpentine along grain boundaries, kelyphite along the edges and fractures of garnet, and a rusty orange alteration mineral/aggregate (iddingsite?) affecting some olivines near the contact with kimberlite.

3.1.3 Pipe 200 Xenolith

The harzburgite xenolith from Pipe 200 (Fig. 3.3) consists of coarse-grained orthopyroxene and olivine (~1.9 to 4.3 mm average diameter), with minor or accessory garnet and diopside, accessory phlogopite and a variety of finer-grained materials forming pockets and a semi-continuous vein. All major and minor phases are mainly anhedral. Olivine contains abundant fractures (Fig. 3.3 A-C) and planar arrays of fluid inclusions, and features minor degrees of grain size reduction along its margins throughout the sample. Secondary minerals (apart from phases appearing in the vein and

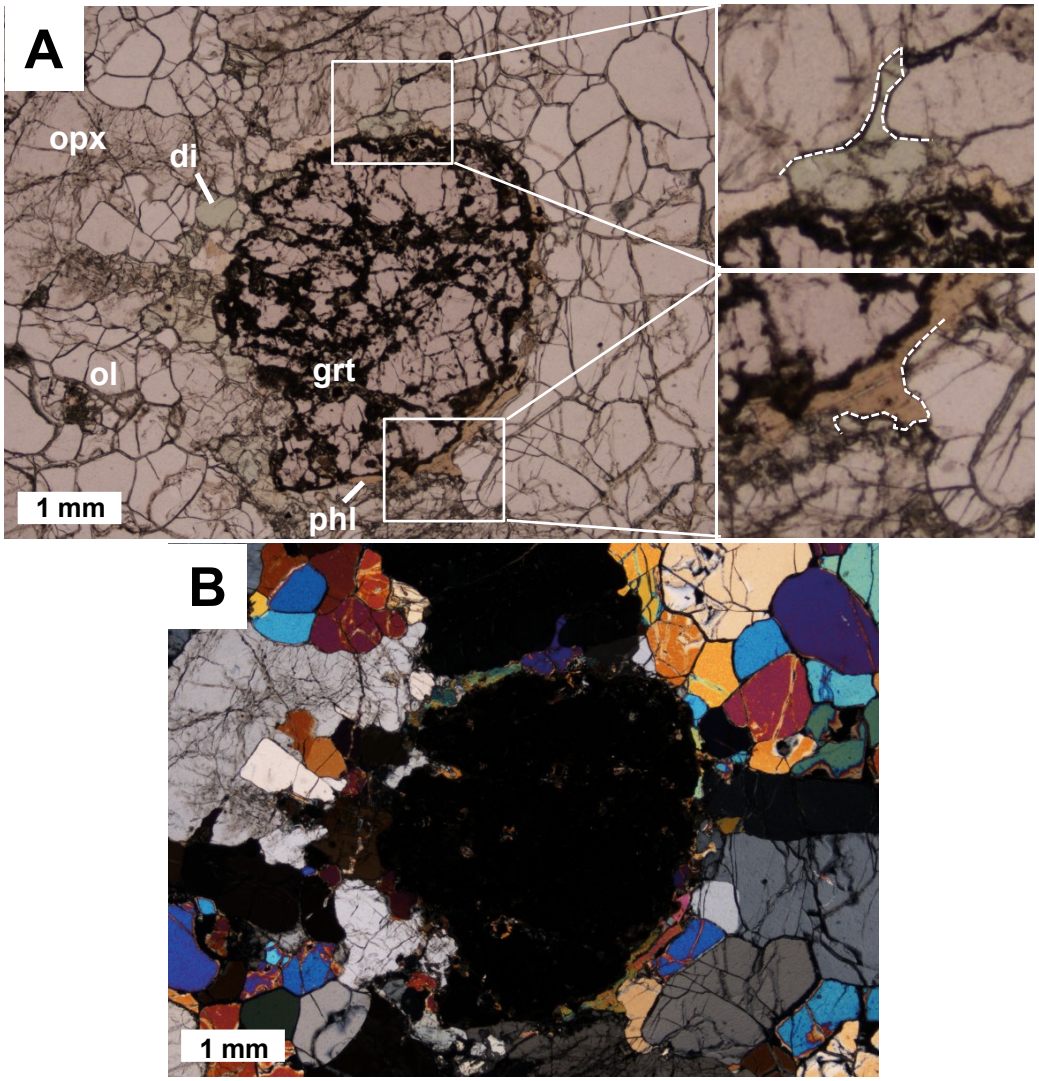

Figure 3.2: Representative images of the Matsoku xenolith. (**A**) Plane-polarized light image of anhedral and subhedral olivines surrounding larger orthopyroxenes and garnets. Phlogopite (orange) and diopside (pale green) surround corroded, partially kelyphitized garnet. *Insets* show interstitial shapes of diopside and phlogopite relative to olivine. **(B)** Cross-polarized image of (**A**). ***di*** – diopside, ***grt*** – garnet, ***ol*** – olivine, ***opx*** – orthopyroxene, ***phl*** – phlogopite.

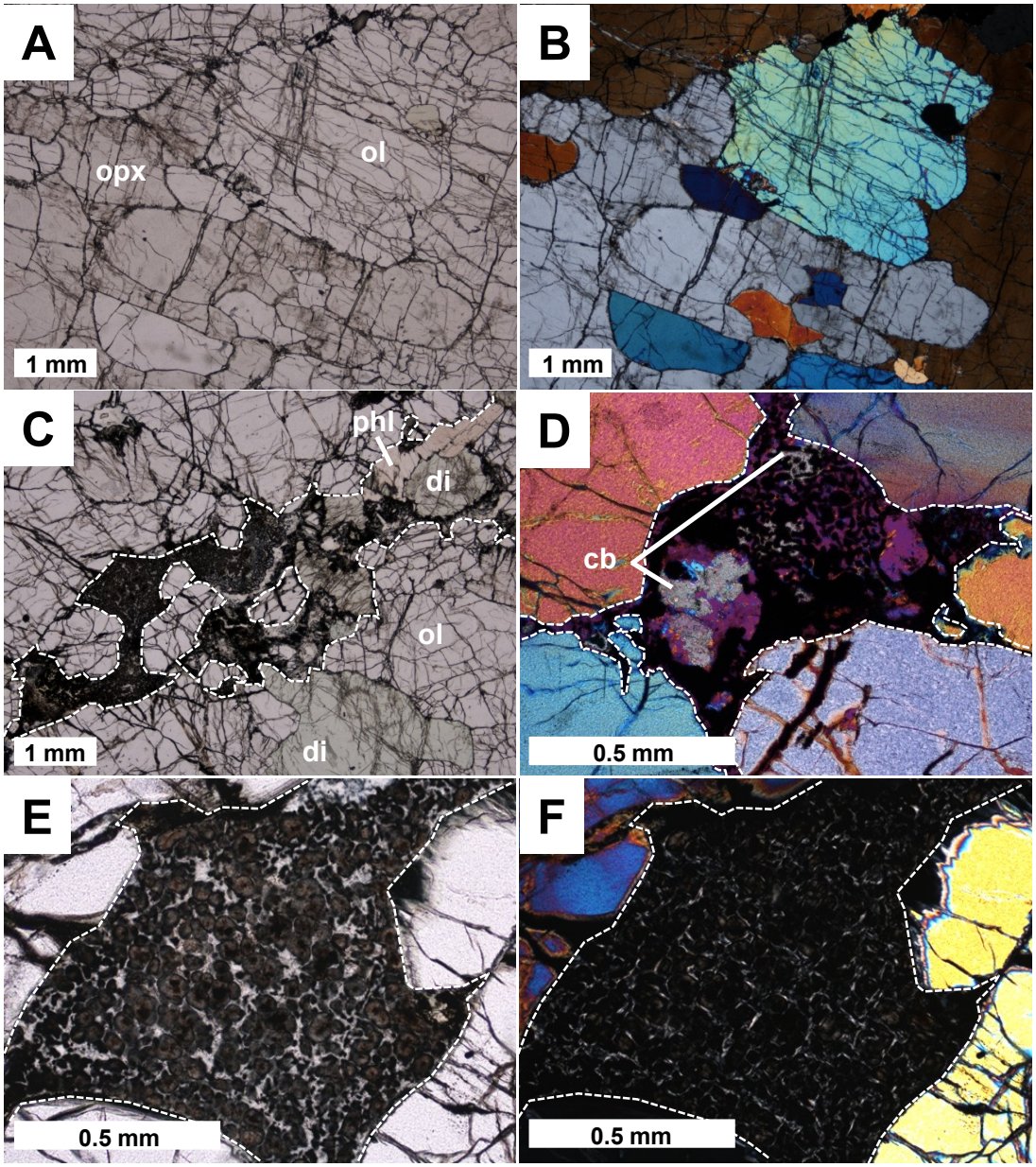

Figure 3.3: Characteristics of the Pipe 200 xenolith. **(A**, **B)** Coarse-grained, sub- to anhedral olivine and orthopyroxene comprise most of the sample. **(C)** A semi-continuous vein consisting of diopside, phlogopite, and cryptic materials intrudes the sample. **(D-F)** Cryptic vein and pocket-forming materials have heterogeneous textures, including: segregations of carbonate with isotropic, crystallite-bearing material **(D)**; irregular intergrowths of carbonate, opaque minerals, and isotropic material **(D)**; and brown spherule-like aggregates surrounded by transparent minerals **(E**, **F)**. In all images dashed lines delineate approximate vein-host contacts. Images include plane **(A**, **C**, **E)** and cross-polarized **(B**, **D**, **F)** light photographs, with **(D)** and without **(B**, **F)** a sensitive tint plate. ***cb*** – carbonate, ***di*** – diopside, ***ol*** – olivine, ***opx*** – orthopyroxene, ***phl*** – phlogopite.

pockets), include serpentine along grain boundaries and fractures, and chlorite replacing an orthopyroxene grain near the kimberlite contact.

The vein (Fig. 3.3 C, E, F) consists of a variety of minerals, including phlogopite, diopside, carbonate, spinel (near garnet contacts), and a variety of unidentified fine-grained to cryptocrystalline and possibly amorphous materials. These latter materials, which also form pockets throughout the xenolith, comprise weakly birefringent minerals, isotropic materials (glass?), and opaque minerals (Fig. 3.3 C-F). The textures and distributions of the vein-forming materials vary widely, and include but are not limited to: segregations of carbonates and isotropic, crystallite-bearing material (Fig. 3.3 D); irregular segregations of opaque minerals intergrown with carbonates and isotropic material (Fig. 3.3 D); and brown spherule-like aggregates in a low birefringence matrix (Fig. 3.3 E, F). The vein does not abruptly truncate xenolith minerals at their contacts; the vein materials commonly have interstitial textures with respect to the primary minerals (Fig. 3.3 C). Distal pockets are connected to the vein by an unidentified orange to grey, isotropic material (serpentine?) along grain boundaries; this material also exists in the vein and pockets.

3.2 Compositions of Olivine

Olivines from all xenoliths (Table 3.1) have restricted Mg# from 92.0 to 92.7, and are poor (< 0.1 wt. % oxide) in most trace elements except for Ni (0.37 to 0.38 wt. % NiO) (Fig. 3.4 A, Table 3.1). Apart from bright rims visible in backscattered electron images of Jericho xenolith olivines, the olivines appear to be homogeneous within each sample.

Macrocrysts (Fig. 3.4 A, Table EA1) are also poor in trace elements other than Ni, with only MnO > 0.1 wt. % in some crystals. Beartooth macrocrysts range from 89.9 to 93.0 in molar Mg#, and 0.26 to 0.36 wt. % in NiO. Late overgrowth rims, which are usually present on olivine macrocrysts in kimberlite, are present on three of 25 macrocrysts observed using backscattered electron imaging, and are laterally discontinuous (Fig. 3.4 B). I could not obtain reliable analyses of these thin (< 50 μm) rims owing to X-ray scattering effects related to the topography of the manually polished grains. Jericho macrocryst cores (n = 7) range in Mg# from 87.60 to 92.13, and from 0.16 to 0.39 wt. % NiO. Typical overgrowth rims of ~100 μm thickness are present on the

Jericho macrocrysts (Fig. 3.4 C): the rims (n = 8) are nearly uniform in Mg# (89.7 to 90.0) and variable in NiO (0.11-0.31 wt. %).

3.3 Infrared Spectroscopy of Xenolith Olivines

The Electronic Appendix contains all spectra from xenolith olivines collected in this study, and the results of data processing of those spectra (Table EA2). Infrared spectra of olivines from each xenolith consist of Group 1 OH absorption peaks over the range of 3000-3700 cm^{-1}. Spectrum types include type A1 (both Jericho xenoliths) and types transitional between A and B (Matsoku and Pipe 200 xenoliths) (Fig. 3.5). (Spectra in

Table 3.1: Compositions of xenolith olivines. *ND* - none detected. *2SD* - two standard deviations.

	Jericho 011		**Jericho 53**		**Matsoku**		**Pipe 200**	
	n = 5	*2SD*	*n = 8*	*2SD*	*n = 6*	*2SD*	*n = 5*	*2SD*
Weight % Oxides								
SiO_2	41.40	0.13	41.35	0.30	40.87	0.25	41.49	0.16
Cr_2O_3	ND		ND		0.018	0.016	0.019	0.006
FeO	7.14	0.12	7.80	0.11	7.44	0.22	7.13	0.08
MnO	0.078	0.008	0.096	0.004	0.089	0.006	0.085	0.009
NiO	0.367	0.014	0.384	0.014	0.385	0.014	0.390	0.007
MgO	50.88	0.27	50.45	0.20	50.01	0.37	50.75	0.49
CaO	0.011	0.007	0.010	0.006	0.026	0.015	0.022	0.003
Na_2O	ND		ND		0.009	0.003	0.006	0.006
P_2O_5	ND		ND		0.013	0.006	0.016	0.020
Total	99.88	0.36	100.11	0.39	98.88	0.47	99.91	0.41
Cations ($4O^{2-}$ basis)								
Si	1.004	0.001	1.003	0.002	1.003	0.002	1.005	0.003
Cr	ND		ND		0.00035	0.00015	0.00036	0.00006
Fe	0.145	0.001	0.158	0.001	0.153	0.002	0.144	0.001
Mn	0.00160	0.00008	0.00197	0.00005	0.00185	0.00007	0.00174	0.00010
Ni	0.00716	0.00014	0.00749	0.00015	0.00759	0.00014	0.00761	0.00007
Mg	1.839	0.002	1.825	0.003	1.829	0.005	1.833	0.006
Ca	0.00029	0.00009	0.00025	0.00008	0.00068	0.00020	0.00056	0.00004
Na	ND		ND		0.00043	0.00006	0.00030	0.00015
P	ND		ND		0.00028	0.00007	0.00034	0.00020
Mg #	92.70	0.06	92.01	0.05	92.29	0.11	92.70	0.05

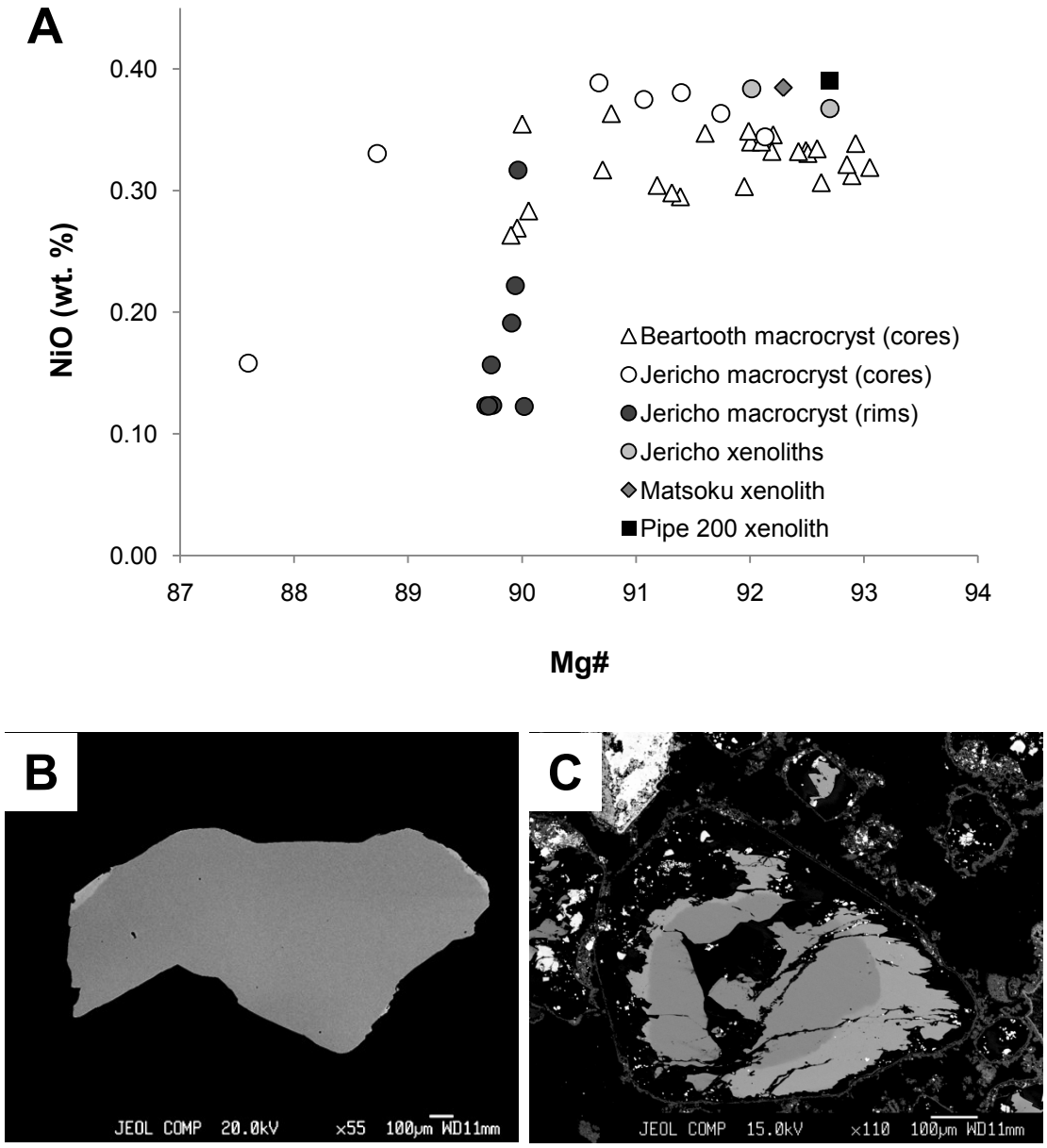

Figure 3.4: Compositions and chemical zonation of xenolith and macrocryst olivines. (**A**) Mg# *vs*. NiO plot illustrating the restricted range of xenolith olivine compositions, more variable range of macrocryst compositions, and constant Mg# of rims on Jericho olivines. (**B**) Backscattered electron image illustrating the thin and discontinuous rims on Beartooth macrocrysts. (**C**) Backscattered electron image illustrating comparatively wider and more continuous rims of Jericho macrocrysts. A variable-thickness pseudomorph partially replaces this macrocryst.

Figure 3.5 represent randomly oriented crystals, and consequently do not necessarily compare well to the (010) spectra presented in Figure 1.2 for classification purposes). Spectrum type is similar in all olivines within the same xenolith, apart from differences resulting from the variable crystallographic orientations of the crystals.

Jericho xenolith olivine spectra (Fig. 3.5) consist of prominent overlapping peaks at ~3571 and ~3578 cm^{-1}, and a strongly pleochroic, sharp peak at 3612 cm^{-1}. Additional peaks include two overlapping peaks at ~3597 and 3590 cm^{-1}, a peak at ~3555 cm^{-1} with a broad, asymmetric shoulder (hidden peak?) down to ~3540 cm^{-1}, as well as low intensity peaks at ~3623 and ~3639 cm^{-1}. A set of three low intensity peaks reside at ~3499, ~3478 and ~3455 cm^{-1}, and weak, broad peaks are present at ~3405 and ~3374 cm^{-1}. These latter two peaks are distinct from proper Group 2 peaks, which consistently reside at ~3356 and 3327 cm^{-1} (11).

Spectra from Matsoku xenolith olivines (Fig. 3.5) differ from the Jericho olivines in that the peak at ~3612 cm^{-1} is weak, the prominent peak at ~3571 cm^{-1} does not overlap with any peak at 3579 cm^{-1}, and peaks at ~3534 and 3523 cm^{-1} are commonly prominent. Triplet peaks from ~3499-3455 cm^{-1} are absent, as are low intensity peaks at ~3405 and ~3374 cm^{-1}. The peak at ~3639 cm^{-1} is stronger relative to other prominent peaks in Matsoku olivines.

The strongest peaks in Pipe 200 xenolith olivines (Fig. 3.5) are generally those at ~3571, ~3593, ~3639, and ~3534 cm^{-1}. The 3523 cm^{-1} peak, where present, is weaker than in Matsoku olivines.

Some spectra from olivines in each xenolith feature a sharp peak at ~3672 cm^{-1}, and a broad, variably asymmetric peak at ~3690 cm^{-1}. The former represents inclusions of talc (33-35, 54), whereas the other represents serpentine, which I believe reside in fractures, inclusion arrays, and grain boundaries (Section 2.3.2).

3.3.1 Zonation of OH Peaks

Zoning trends of xenolith olivines vary among the studied localities (Table 3.2). Zonation of OH-related infrared peaks in olivines from Jericho xenoliths is restricted (Figs. 3.5; 3.6 A, B; 3.9 A). Profiles of integrated Group 1 peak intensities range from flat to weakly curved upward or downward in the margins of the crystals (Fig. 3.6 A, B). Such within-crystal variations typically fall within estimated uncertainties, although a few crystals

Table 3.2: Summary of OH peak zonation in xenolith and macrocryst olivines.

Sample type	$r_{A_{int}}$			
Xenolith	*Minimum*	*Mean*	*Maximum*	*N*
Jericho 011	0.87	1.02	1.19	9
Jericho 53	0.75	0.99	1.34	11
Matsoku	0.18	0.43	0.63	9
Pipe 200	0.25	0.48	0.65	6
Macrocryst				
Jericho	0.77	0.96	1.04	7
Pipe 200	0.26	—	0.52	2
Beartooth				
Group 1	0.43	0.90	1.15	100
Group 2	0.13	0.75	1.19	63

show moderate increases or decreases in integrated peak intensity that exceed estimated uncertainty (*e.g.*, Fig. 3.5 B). The ratio ($r_{A_{int}}$) between integrated peak intensity (A_{int}) in the rim and core,

$$r_{A_{int}} = \frac{A_{int}^{rim}}{A_{int}^{core}}, \quad (3.1)$$

represents the magnitude of zonation in a given crystal. The ratio $r_{A_{int}}$ ranges from 0.87 to 1.18 in sample 011 (mean = 1.02, n = 9), and from 0.74 to 1.34 in sample 53 (mean = 0.99, n = 11).

Olivines from the Matsoku and Pipe 200 xenoliths consistently show gradational decreases in integrated Group 1 peak intensities from core to rim that fall well outside of estimated uncertainties (Figs. 3.5; 3.6 C, D; 3.9 B). These trends are undisturbed by fractures or veins of serpentine that cut across some of the olivines. The ratio $r_{A_{int}}$ varies from 0.18 to 0.63 in Matsoku olivines (mean = 0.43, n = 9), and from 0.25 to 0.65 in Pipe 200 olivines (mean = 0.48, n = 6).

The degree of H zonation (*i.e.*, $r_{A_{int}}$) shows no strong correlation with position in the xenolith or mean grain diameter (Fig. 3.7). Crystals in direct contact with surrounding kimberlite commonly have equally profound or restricted zoning as those protected in the core of the xenolith.

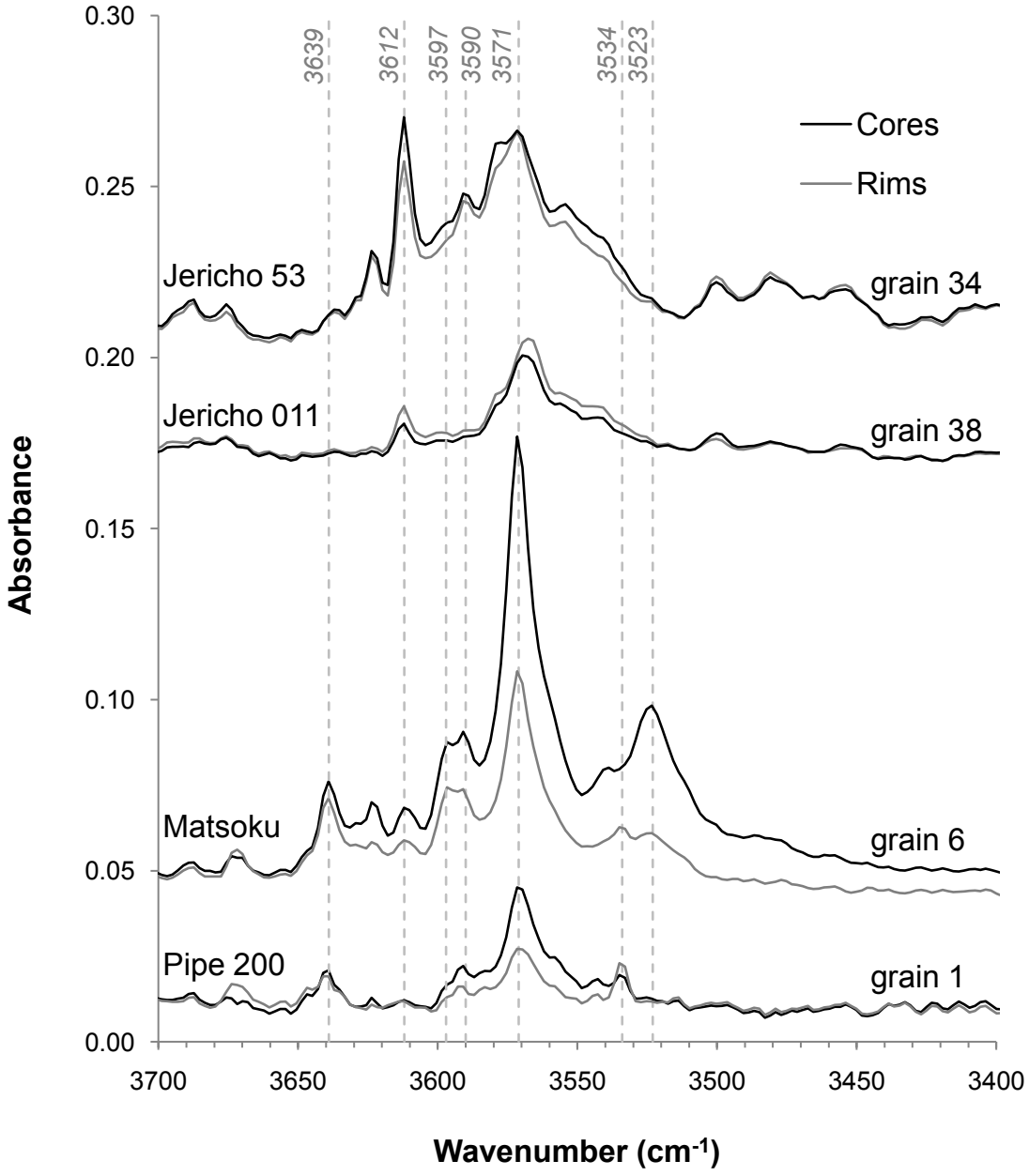

Figure 3.5: Infrared absorption spectra of randomly oriented xenolith olivines. Spectra show differences in OH peak intensities between cores (*black curves*) and rims (*grey curves*). Some peaks attenuate more profoundly in rims than others (*e.g.*, peak ~3571 cm^{-1} in grain 1, Pipe 200). *Vertical dashed lines* represent wavenumbers of selected peaks mentioned in the text.

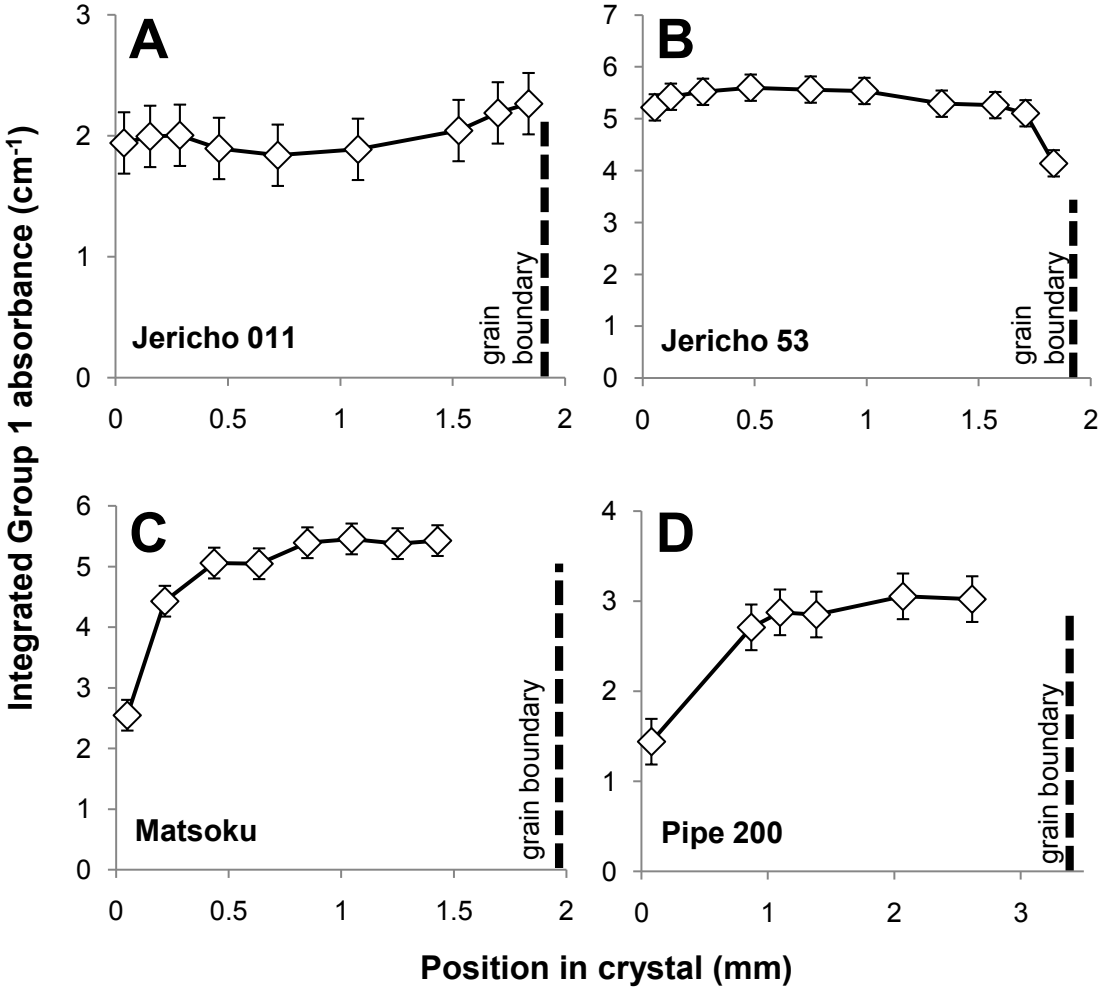

Figure 3.6: Representative profiles of integrated Group 1 peak intensity across xenolith olivines. (**A**) Jericho sample 011. (**B**) Jericho sample 53. (**C**) Matsoku. (**D**) Pipe 200. Jericho olivines show limited (**A**, **B**) variation in Group 1 OH peak intensities, whereas Matsoku and Pipe 200 (**C**, **D**) olivines show profound H depletion in rims. *Vertical dashed lines* and $x = 0$ mark grain boundaries.

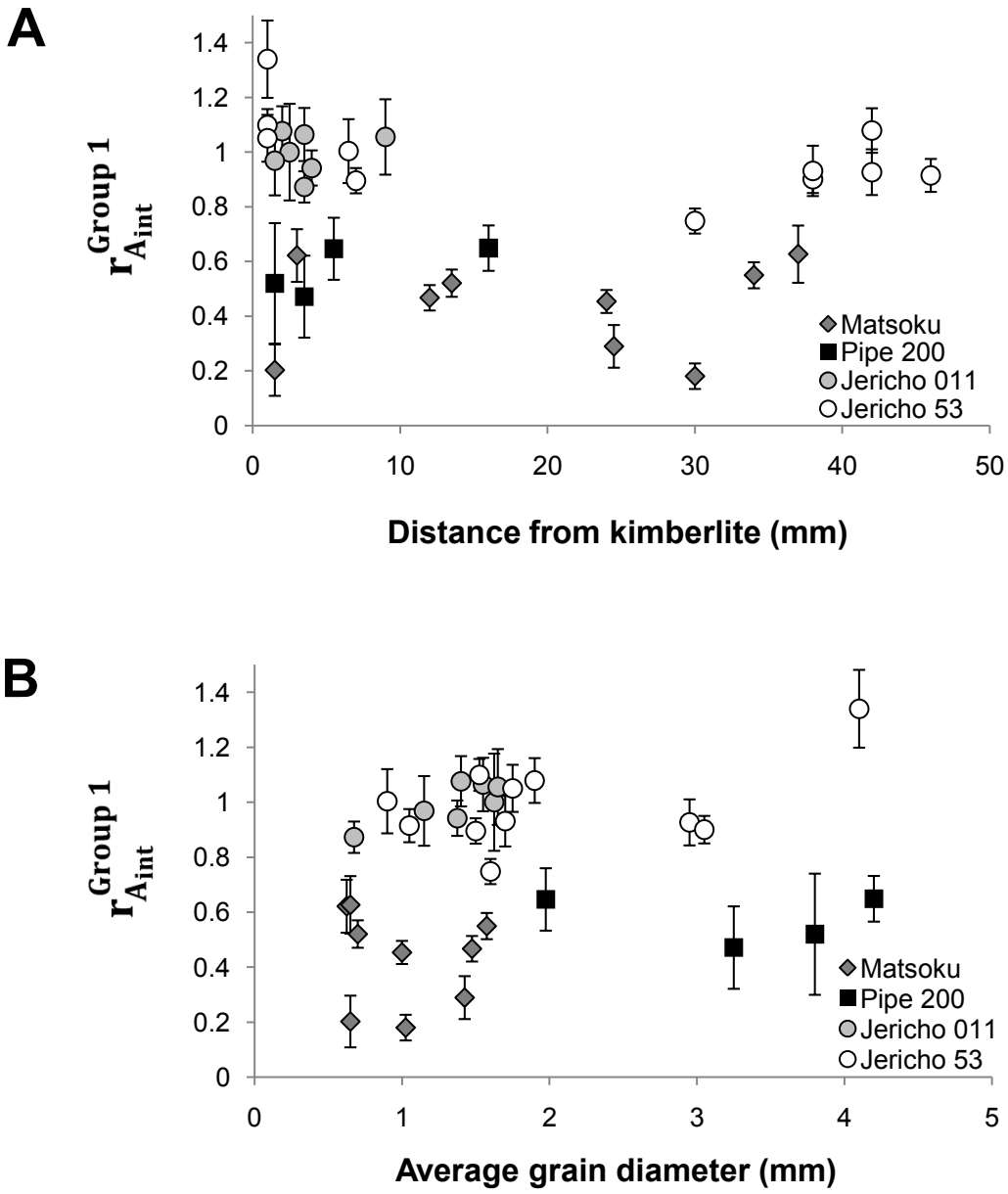

Figure 3.7: Hydrogen-zonation as a function of distance from the kimberlite and grain size. (**A**) Position of olivine relative to kimberlite shows no correlation with the zonation ratio of Equation 3.1. (**B**) Zonation also shows no relationship to mean grain diameter.

Where overall Group 1 OH peaks decrease in intensity in the rims of Matsoku and Pipe 200 olivines, relative peak intensities of specific peaks also may vary within single crystals. For example, in the core and rim spectra (Fig. 3.5), certain peaks attenuate substantially in rims, whereas others retain similar height or even intensify relative to those observed in the cores. In the Matsoku example, peaks at ~3571 and ~3523 cm^{-1} decrease substantially in height, whereas ~3639 and ~3590-3597 cm^{-1} maintain similar heights relative to the apparent baseline. Similarly, the Pipe 200 example shows no intensity change of peak ~3639 cm^{-1}, substantial decreases in peak ~3570 cm^{-1}, and a moderate increase in peak ~3534 cm^{-1}.

Zonation patterns of Group 1 H in xenolith olivines appear to reflect the diamond grade of the host kimberlite (Fig. 3.9 D, E). Strongly zoned olivines are associated with diamond-poor Matsoku (J. Gurney, pers. comm., 2011) and Pipe 200 kimberlites (56) whereas the diamondiferous Jericho kimberlite (*e.g.* 59) contains weakly zoned xenolith olivines.

3.4 Infrared Spectroscopy of Olivine Macrocrysts

The Electronic Appendix contains all spectra from olivine macrocrysts collected in this study, and the results of data processing of those spectra (Table EA2). Group 1 peak-bearing macrocrysts exist in olivine populations from each locality studied here, whereas only those from the Beartooth kimberlite contain Group 2 peaks. Therefore, I describe types and zonation of Group 1 peaks separately from Group 2 peaks in the following sections.

3.4.1 Group 1 Peaks

The Group 1 regions of macrocryst infrared spectra reported in this study generally fall into the classification scheme in Figure 1.2. The 101 Beartooth olivines analyzed include all Group 1 types, and all except Group 1C exist in the 23 Jericho macrocrysts. Many of the 13 macrocrysts from Pipe 200 are difficult to classify owing to their low peak intensities; where peaks are sufficiently intense to allow classification, spectra resemble the Group 1C type.

Group 1 peaks in macrocrysts also exhibit variable degrees of zonation (Table 3.2). Jericho macrocrysts span a wide range of integrated intensities (*i.e.*, areas beneath Group 1 peaks) from negligible to 16.5 cm^{-1}, but exhibit restricted zoning (Figs. 3.8,

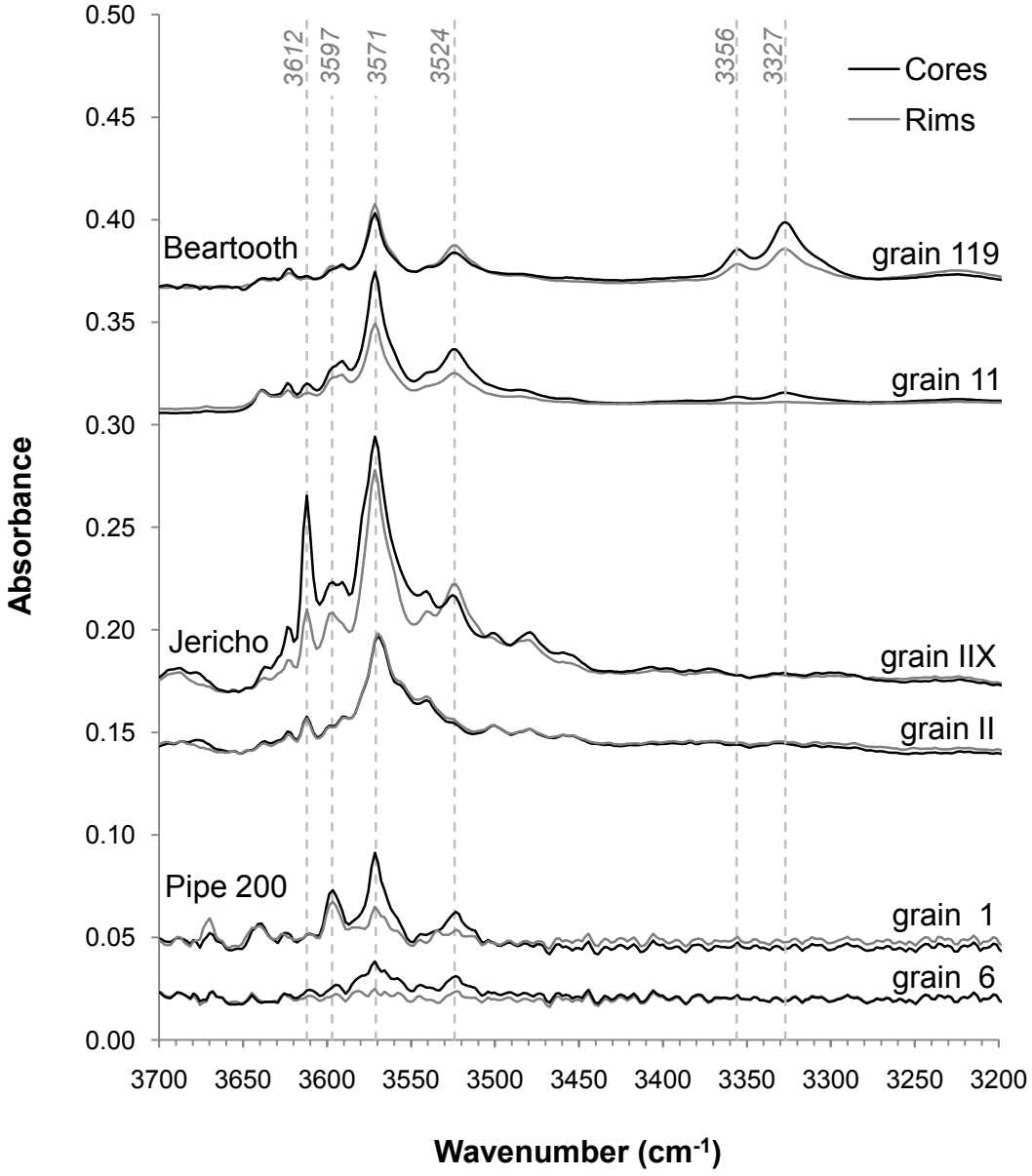

Figure 3.8: Infrared absorption spectra of randomly oriented olivine macrocrysts. Spectra show differences in OH peak intensities between cores (*black curves*) and rims (*grey curves*). Zonation ranges from negligible (Jericho, grain II) to substantial (Pipe 200, grains 1 and 6). Zonation of Group 1 peaks (3450-3650 cm^{-1}) is typically less profound than that of Group 2 peaks (3300-3400 cm^{-1}; Beartooth, grains 11 and 119). Some peaks in the Group 1 region attenuate more profoundly than others in the rims (*e.g.*, peak 3612 cm^{-1}; Jericho, grain IIX). Spectra are not thickness normalized. *Grey dashed lines* mark selected wavenumbers mentioned in the text.

3.9A). Zonation ranges from $r_{A_{int}}$ of 0.77 to 1.04 (mean = 0.96, n = 7). Beartooth macrocrysts show a similar range of integrated Group 1 intensities (negligible to 12.5 cm^{-1}) and a broader, although similar on average, degree of zonation ($r_{A_{int}}$of 0.42-1.15, mean = 0.90, n = 100) (Figs. 3.8, 3.9C). Pipe 200 macrocrysts have low integrated peak intensities (negligible to 1.8 cm^{-1}) and, where cores and rims could be analyzed, strong zonation ($r_{A_{int}}$ of 0.26 and 0.52, n = 2). Zoning trends in macrocrysts from Jericho and Pipe 200 mimic those of xenolith olivines from the same kimberlite (Fig. 3.9 A, B).

Like xenolith olivines, some zoned macrocrysts also exhibit relative changes in heights of specific peaks. For example, Jericho grain IIX (Fig. 3.8) shows restricted changes in most peaks in the rim, but a substantial decrease in intensity of peak ~3612 cm^{-1}. Similarly, grain 1 from Pipe 200 shows nearly complete attenuation of peaks ~3571 and ~3524 cm^{-1} in the rim, whereas peak ~3597 cm^{-1} retains a similar intensity to that of the core.

Zonation of Group 1 H in olivine macrocrysts appears to correlate with the diamond grade of the host kimberlite (Fig. 3.9 D). Olivines from the diamondiferous Beartooth and Jericho kimberlites (*e.g.*, 8, 59, 62) are typically weakly zoned, whereas the two Pipe 200 (diamond-poor kimberlite (56)) macrocrysts are strongly zoned.

3.4.2 Group 2 Peaks

Among all samples examined in this work, Group 2 peaks (peaks at ~3356 and ~3327 cm^{-1}) exist only in olivines from the Beartooth kimberlite. Group 2 peaks can be present *or* absent in olivines of any Group 1 type, including rare grains with virtually no Group 1 peaks. Group 2 peaks are usually less intense than Group 1 peaks, with the A_{int} ratio of Group 2/Group 1 exceeding unity in only three grains, each of which has unusually weak Group 1 peaks. The integrated peak intensities range from negligible to 1.2 cm^{-1}.

As with Group 1 peaks, some Beartooth olivines are zoned with respect to Group 2 peaks (Table 3.2, Fig. 3.10). Group 1 and Group 2 peaks are commonly zoned within the same crystals, although some crystals exhibit zoning of Group 1 or Group 2 peaks without variation in the other (horizontal and vertical lines in Fig. 3.10, respectively). Group 2 $r_{A_{int}}$ ranges from 0.13-1.19 (mean = 0.75, n = 63). In a proportional sense, Group 2 bands tend to be better attenuated in rims relative to cores than Group 1 bands; *i.e.*, $r_{A_{int}}$ of Group 2 bands is usually smaller than for Group 1 bands within strongly

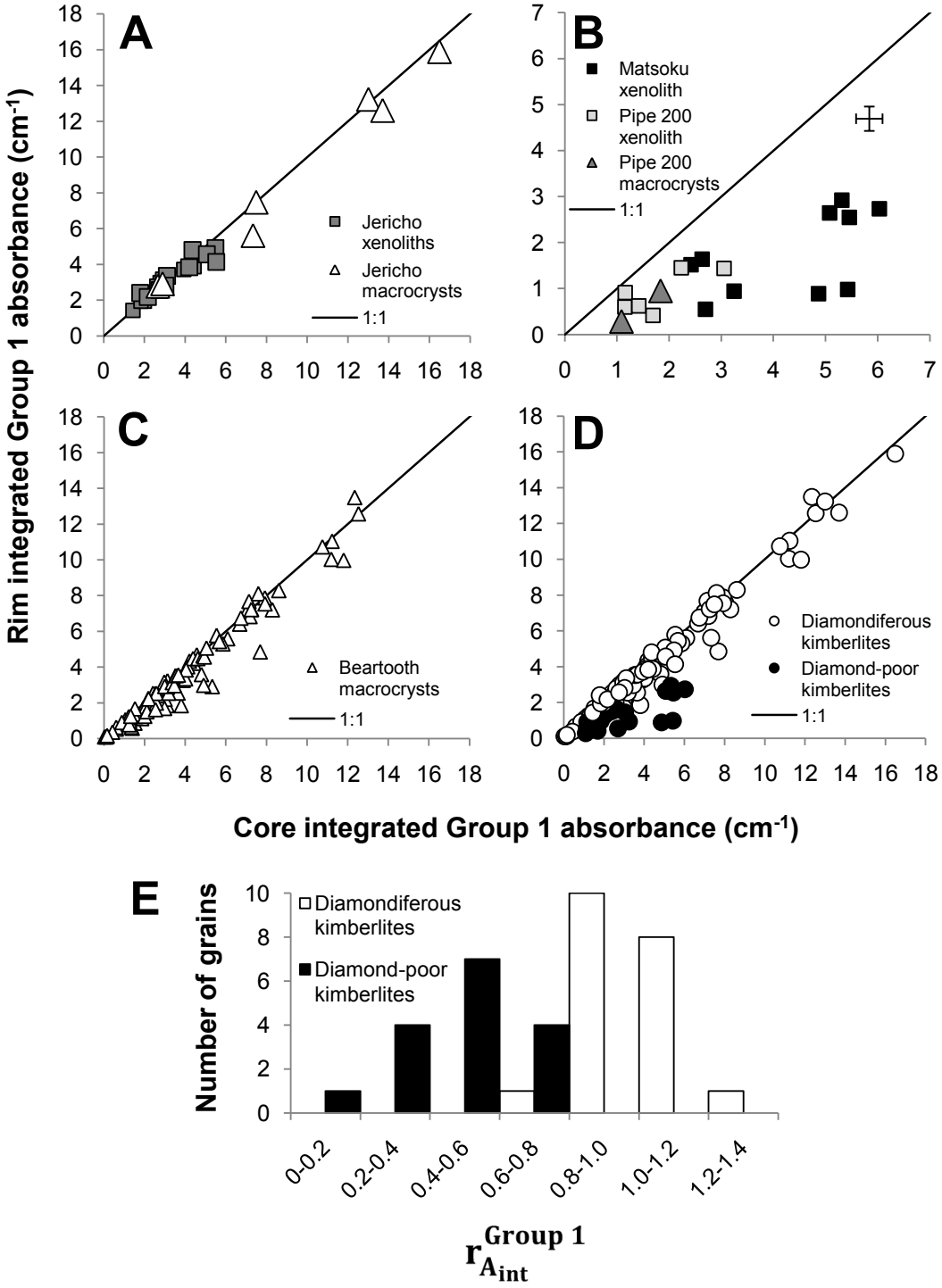

Figure 3.9: Plots illustrating Group 1 peak zonation in kimberlite-related olivines. (**A**) Jericho olivines. (**B**) Southern African olivines. (**C**) Beartooth macrocrysts. (**D**) Comparison of diamondiferous and diamond-poor kimberlites. (**E**) Histogram of rim:core zonation ratios of xenolith olivines from the diamondiferous and diamond-poor kimberlites. In **A**, **C**, and **D**, estimated uncertainties are within the symbols.

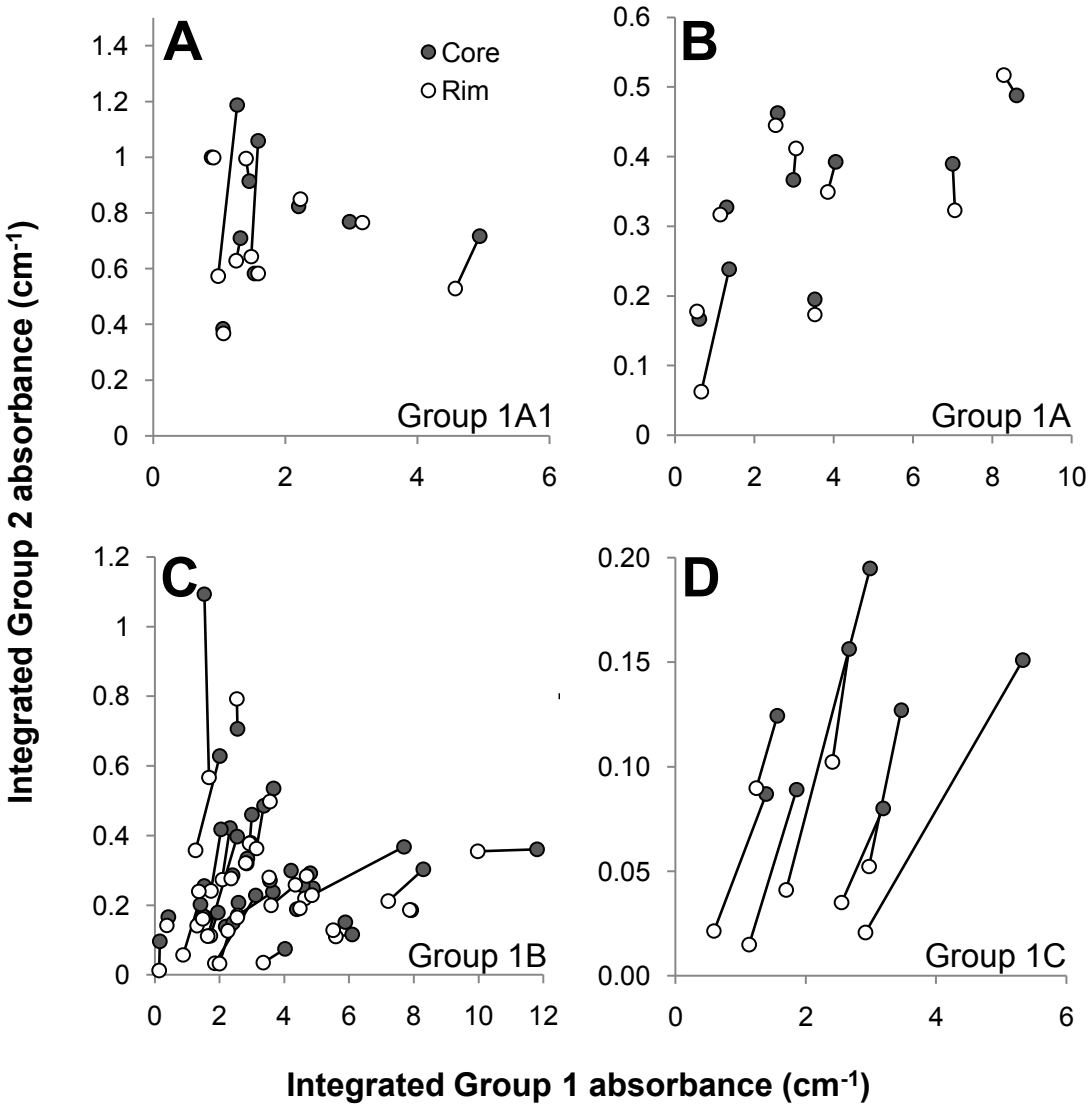

Figure 3.10: Variation of the integrated intensities of Group 1 and Group 2 peaks between the cores and rims of Beartooth macrocrysts. (**A**) Group 1A1 spectra. (**B**) Group 1A spectra. (**C**) Group 1B spectra. (**D**) Group 1C spectra. In general, rims of zoned crystals are relatively depleted in both Group 1 and Group 2 H. Few crystals show increasing H content in rims, or zonation of Group 1 H independent of Group 2 H, or *vice versa.*

zoned crystals (Fig. 3.11).

3.5 Summary

Olivines in peridotite xenoliths from the kimberlites Jericho, Pipe 200, and Matsoku exhibit contrasting degrees of H zonation, but have similar chemical compositions. Crystals from the Pipe 200 and Matosku xenoliths show persistent decreases in Group 1 H in their rims relative to the Jericho xenolith olivines. Macrocrysts from Beartooth and Jericho have a wider range of chemical compositions then the xenolith olivines. Macrocrysts from Jericho and Pipe 200 show similar H zonation trends to the xenolith olivines from the same kimberlite. Beartooth macrocrysts, which feature both Group 1 and Group 2 H-bearing olivines, typically exhibit restricted zonation of Group 1 H and more profound zonation of Group 2 peaks. Zonation of Group 1 H in xenolith and macrocrystic olivines appears to correlate with the diamond grade of the host kimberlites.

In the next chapter, I discuss the possible origins of H zonation, and the physical and chemical parameters that could produce inter-locality variation. I also discuss how these parameters could influence the extent of diamond resorption during ascent in kimberlite magmas. I discuss possible reasons for the differential zonation of Group 1 and Group 2 H in the Beartooth olivines, and how this phenomenon may explain the distribution of Group 2-bearing olivines in Lac de Gras kimberlites. I conclude with suggestions of future research projects that could test the hypotheses that stemmed from this work.

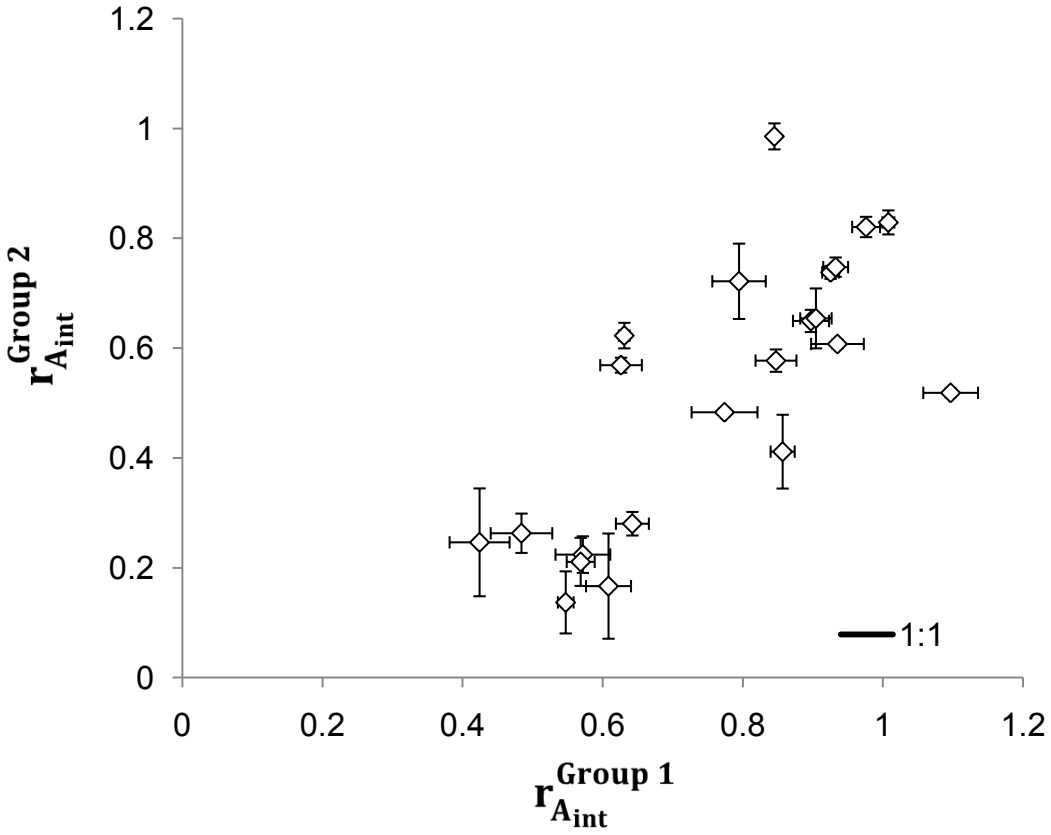

Figure 3.11: Comparison between the zonation ratios ($r_{A_{int}}$) of Group 1 and Group 2 peaks in strongly zoned Beartooth olivines. Most crystals fall below the 1:1 line, indicating preferential depletion of Group 2 H.

CHAPTER 4

DISCUSSION

4.1 Summary of H-Zonation in Kimberlite-Hosted Olivine

This study and earlier works (17, 23, 48, 52) show that H zonation in kimberlite-hosted olivines varies among different intrusions. Xenolith and macrocrystic olivines from the Jericho and Beartooth kimberlites show minor zonation of Group 1 H, whereas crystals from the kimberlites Pipe 200 and Matsoku show profound depletion of these H defects in their rims (Figs. 3.5, 3.6, 3.8, and 3.9). The degree of peak attenuation differs among different defects; Group 2 peaks (Beartooth only) typically attenuate more strongly than Group 1 peaks (Fig. 3.11), and certain peaks (*e.g.*, 3600 cm^{-1}) within the Group 1 region are less attenuated than others (*e.g.*, 3571, 3524 cm^{-1}) within the same individual crystals (Figs. 3.5, and 3.8). The degree of Group 1 H depletion in xenolith and macrocrystic olivines correlates with the abundance of diamond in the host kimberlite (Fig. 3.9 D, E), indicating that H zonation may be a cost-effective tool for evaluating the diamond potential of new kimberlite discoveries. In this chapter, I describe the possible (and probable) explanations of the zonation phenomena, their significance for water in kimberlites, and why they may correlate with diamond grade. I also propose future research projects that could further test the practical applications, and better elucidate the causes of zonation patterns.

4.2 Possible Origins of H-Zonation

In general, the olivines examined in this study feature either no H zonation, or depletion of H in their rims. Decreasing H trends could develop during crystal growth in an environment in which the equilibrium concentration of H decreased during growth, perhaps as a result of changing H_2O-CO_2 ratio or decreasing fluid pressure (15, 16, 47). However, xenolith olivines that feature H zonation are homogeneous with respect to other elements. Given the fast diffusion rates of H in olivine (13, 14), growth zonation of H could not be preserved without preservation of growth zones of slower-diffusing cations (*e.g.*, Fe^{2+}, Mg^{2+} (63)). Thus, growth zoning of H probably does not contribute to the H depletion patterns in the xenolith olivines. In the case of olivine macrocrysts, growth zoning may be more important; macrocrysts commonly have chemically distinct

rims overgrown onto homogeneous cores of lower or higher Mg# (*e.g.*, Fig. 3.4 C) (2, 18, 19, 29, 32). Thus, relative H-depletion in the rims of Pipe 200, and (to a lesser extent) Beartooth and Jericho macrocrysts may reflect a combined signal from H-bearing cores and H-poor or anhydrous rims. However, backscattered electron images of selected Beartooth olivines show anomalously thin (< 50 μm), discontinuous rims, or (more commonly) none at all (*e.g.*, Fig. 3.4 B). Thus, their contribution to observed H-zonation in Beartooth crystals is probably minimal. Additionally, in the Jericho macrocrysts, which feature typical overgrowth rims, zonation of H is normally absent. This observation suggests that the contribution of late rims to the observed zonation trends is minimal, and requires that a process other than growth zoning affected the distribution of H in zoned olivine macrocrysts. The apparent irrelevance of overgrowth rims on H zonation in Jericho olivines may be artificial; the spectra obtained from rims of crystals could contain signals both from overgrowths and cores, given that the beam size is large (50x50 μm^2) relative to the thickness of these rims (~100 μm). The typical lack of zoning either reflects a small volume of late rim in the beam path, or a similar H defect signature in the rims and cores.

Other workers interpreted H depletion trends in xenolith olivine rims to have resulted from H diffusion; this interpretation derives from the convex shape of H profiles, and the rapid diffusion rates of H in olivine (13, 14). Such profiles are also present in the xenolith olivines from Pipe 200 and Matsoku (Fig. 3.6 C, D), indicating that diffusive H loss also affected these samples. A diffusive origin seems incompatible with the lack of correlation between grain size and degree of zonation in the xenolith olivines (Fig. 3.7 A). This phenomenon may simply reflect variation in the distance of the outermost analyses relative to the grain boundary, or the dependence of the diffusion coefficient on crystallographic direction (13, 14). Demouchy and Mackwell (14) argued that crystallographic dependence of diffusion produces variable degrees of zonation along different directions in zoned crystals, based on similar comparability of one-dimensional and three-dimension diffusion models with measured zonation profiles. Therefore, the data in Figure 3.7 A do not disprove that diffusion produced the zonation, and this process remains a satisfactory explanation for the zoning. Thus, I interpret the decreasing peak intensities to represent diffusive H-loss.

Diffusive H-loss either occurred during non-kimberlitic processes (such as metasomatism in the mantle or post-ascent hydrothermal alteration), or during transport in kimberlite magma. A hydrothermal origin is unlikely because veins of serpentine associated with this process do not disturb zonation trends; Demouchy *et al.* (50) noted the same phenomenon in H-zoned xenolith olivines from alkali basalt. Metasomatic H loss is also unlikely because high pressures favour high H-solubility in olivine (15, 47), and the timescale of H-diffusion in olivine is short; detectable zonation (such as that observed in Matsoku and Pipe 200 olivines) can be produced in minutes or hours at mantle temperatures (13, 14). Furthermore, the metasomatism associated with the strongly zoned olivines involved a hydrous medium, as evinced by crystallization of phlogopite (Figs. 3.2, 3.3). Thus, metasomatism of these xenoliths probably did not cause diffusive loss of H in the olivines.

If we can rule out metasomatic and hydrothermal H diffusion, the xenolith olivines probably lost H during ascent in magma, as others have invoked to explain H zonation in xenolith olivines from kimberlites and basalts (17, 50, 52, 55). Whether the zoning resulted from equilibration with magma, exsolved fluid, or (in the case of xenolith olivines) pre-kimberlitic intergranular fluid is less clear. The presence of profoundly zoned crystals both in the margins and cores of xenoliths (Fig. 3.7 A) suggests that an intergranular medium interacted with the crystals. Given the absence of quenched kimberlite melt in the interstices of the samples with pronounced zoning, direct loss of H to magma seems unlikely. However, the consistent zoning relationships between xenolith olivines and macrocrysts from the same intrusions suggests that H-diffusion was governed by the activity of water in a common medium, given that the growth zonation of macrocrysts seems to have contributed little to the H-zonation (see above). One possible explanation for this phenomenon is that the surfaces of both macrocrysts and xenoliths served as nucleation loci for fluids (64, 65), which then controlled the equilibrium H-concentration imposed on the olivines; the presence of kelyphite rims on garnets in the Matsoku and Pipe 200 xenoliths, along with the common presence of kelyphitized garnet in kimberlites (2, 66) support this scenario. Regardless of the details of the interaction, my data suggest that the zonation resulted from re-equilibration with a

kimberlitic medium, on the basis of the similar behaviour of macrocrysts and xenolith olivines. Thus, I employ that assumption hereafter.

4.3 Factors Contributing to Diffusive H-Zonation

Changes in any physical or chemical parameter that influences the solubility of H in olivine could result in diffusive exchange of H between olivine and its surroundings. Decreases in pressure (15, 16) or temperature (46) can produce changes in the equilibrium H-concentration. The effect of pressure on H-solubility results from concomitant changes in the fugacities of H_2 and H_2O (15, 16); temperature presumably exerts similar influences. Direct changes in the chemical environment could also change the H-solubility; for example, olivine in equilibrium with a (nominally) pure aqueous fluid would be richer in H than one in equilibrium with a hydrous melt (11, 23). Thus, variation in any combination of temperature, pressure, or chemical environment could produce the H-zonation trends observed.

Below, I explore the effects of temperature and equilibrium H-concentration using diffusion models to provide insights into the origins of contrasting H-zonation trends in olivines from the kimberlites investigated here. These models assume that the diffusion coefficient is independent of pressure, oxygen fugacity, and the composition of olivine, as insufficient experimental evidence exists to evaluate the effects of these parameters. Interpretations of the diffusion models may require adjustment following future studies of these effects.

4.3.1 Effect of Temperature on H-Diffusion

Figure 4.1 illustrates the effect of temperature on $r_{A_{int}}$ (rim:core H concentration ratio) of H-bearing olivine re-equilibrating in an anhydrous environment. I calculated these curves from model diffusion profiles of an initially homogeneous 2 mm olivine grain annealed at 1100, 1200, and 1300 °C, in an environment at equilibrium with anhydrous olivine (hereafter referred to as the 'anhydrous olivine model'), using a Microsoft Excel © spreadsheet. The diffusion profiles derive from the same formulation Peslier *et al*. (17, 52, 55) applied to H diffusion in olivine, based on Shewmon's (67) expression for degassing of a slab in one dimension:

$$C_{X,t} = \frac{4C_0}{\pi}\sum_{j=0}^{\infty}\frac{1}{(2j+1)}\cdot\sin\left\{\frac{[(2j+1)\pi X]}{h}\right\}\cdot\exp\left\{-\left[\frac{\{2j+1)\pi}{h}\right]^2\cdot D\cdot t. \quad (4.1)$$

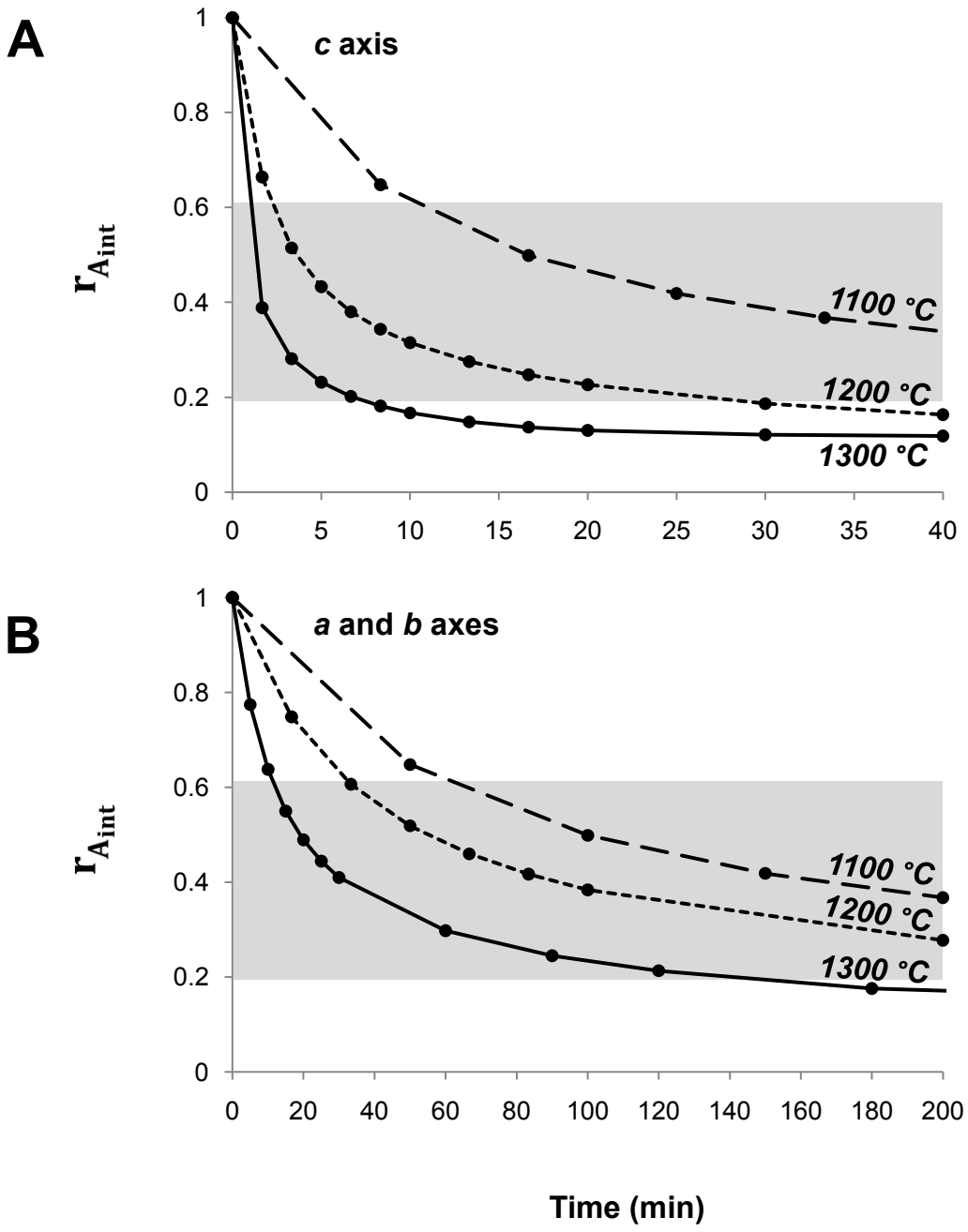

Figure 4.1: Diffusive changes in H zonation in olivine as a function of temperature, time, and crystallographic direction, for H-bearing olivine re-equilibrating with an anhydrous environment. The *y* axis shows the rim:core intensity ratio, $r_{A_{int}}$. The *shaded region* represents the range of values from Matsoku and Pipe 200 olivines. (**A**) Zonation resulting from diffusion along the *c* axis. (**B**) Zonation resulting from diffusion along the *a* and *b* axes.

Here, the concentration ($C_{X,t}$ in arbitrary units) at position X (in m) is a function of the initial H concentration (C_0 in arbitrary units, modeled at 100 ppm), profile width (h in m),diffusion coefficient (D in [m^2·kJ] / [mol·s]), and time (t in s). I calculated the expression to eight terms (it converges after five (17)), and used the following diffusion coefficients:

$$D_{a,b\ axes} = 10^{-4.5}\exp\left(-\frac{204}{RT}\right), \tag{4.2}$$

$$D_{c\ axis} = 10^{-1.4}\exp\left(-\frac{258}{RT}\right), \tag{4.3}$$

where R is the gas constant (0.00831451 kJ/[K·mol]) and T is temperature (in K). Finally, I calculated $r_{A_{int}}$ from the model H-concentrations averaged over the regions 50 to 100 μm from the grain edge, and in the centre of the crystal:

$$r_{A_{int}} = \frac{C^{average}_{at\ 50-100\ \mu m}}{C^{average}_{central\ 50\ \mu m}}. \tag{4.4}$$

These diffusion coefficients were determined from experiments at 0.2 and 1.5 GPa (14), and represent H-diffusion by a vacancy-coupled mechanism (14) that previous workers reasoned applied to diffusion on magmatic timescales (17, 50, 55). A faster mechanism (H and electron holes) that is related to valance changes of Fe produces only minor changes in H content (14). The Appendix describes the sensitivity of the model to the h parameter, and electronic appendix tables EA3 and EA4 contain the model parameters and numerical outputs, respectively.

Hydrogen-bearing olivine undergoing dehydration progressively loses H in its outer margin through to its core as time passes (Fig. 4.1). The ratio $r_{A_{int}}$ initially drops rapidly until leveling off to an asymptote of ~0.118. At constant temperatures of 1100, 1200, and 1300 °C, 20 min of diffusive H loss along the c axis produces $r_{A_{int}}$ values of ~0.4, ~0.2, and ~0.1, respectively; along the a and b axes[1], the respective $r_{A_{int}}$ values are ~0.8, ~0.7, and ~0.5. Thus, contrasting thermal regimes in different intrusions could

[1]The uncertainty in the exponent in Equation 4.2 (diffusion coefficient for the a and b directions) is ± 4.1 (14), which is sufficiently large to produce wide variations in the extent of diffusion at a given time. Therefore, the time axes in Figures 4.1 B and 4.2 B are semi-quantitative, and estimation of diffusion durations along these directions must await more robust experimental determination of the diffusion coefficient.

explain the differing $r_{A_{int}}$ values of their olivines. That is, the greater loss of H from the Pipe 200 and Matsoku olivines could have resulted from higher temperatures of these magmas, in comparison with those of Jericho and Beartooth. Similarly, differing ascent durations in the same thermal regime could also explain these variations.

Estimates of magma ascent duration, which are based on diffusive Ar-loss of phlogopite and reaction rim thicknesses on garnet xenocrysts, range from ~1 to 24 hr at an assumed temperature of 1100 °C (6, 66, 68). These durations are sufficiently long to allow profound diffusive H loss along the *c* axis in the anhydrous environments implicit in Figure 4.1; after 1 hr, $r_{A_{int}}$ drops to ~0.3, whereas after ~8 hr values approach the asymptote. For the *a* and *b* axes, $r_{A_{int}}$ reaches ~0.2 by 24 hr. Thus, although 24 hr is too long to produce the average $r_{A_{int}}$values the Matsoku and Pipe 200 olivines (0.41 and 0.53, respectively), the anhydrous olivine model reasonably matches the shorter published ascent durations, assuming that the kimberlite magma incorporated garnets, phlogopites and olivines at similar depths.

Despite the reasonable agreement between measured $r_{A_{int}}$ values from Matsoku and Pipe 200, those predicted from the anhydrous olivine model, and published ascent times, the apparently elevated water content in kimberlite magmas (1, 2, 8, 11, 23) limits the applicability of this model to kimberlitic olivine. This inapplicability is evident because the typical $r_{A_{int}}$ of the Jericho and Beartooth olivines (~0.9) requires extremely short durations (< 2 and < 10 min for fast and slow directions, respectively) at 1100 °C in the anhydrous olivine model. Given that kimberlite magmas experience temperatures of ~1100 °C during crystallization of relatively late olivine rims (29), and probably begin at temperatures of in excess of 1300 °C (5), the model temperature of 1100 °C must underestimate the dehydration duration. The short dehydration durations required by the restricted degrees of H-loss in the Jericho and Beartooth olivines seem unrealistic even at the conservative temperature of 1100 °C, and would shorten at higher temperatures (Fig. 4.1). Therefore, we must consider the effects of elevated equilibrium H concentrations on diffusive H-zonation to understand its tendency to vary among different intrusions.

4.3.2 Effect of Chemical Environment on H-Diffusion

In light of the probability that the anhydrous olivine model is inapplicable to kimberlites, I examined the effect of imposed equilibrium H concentrations on the ratio $r_{A_{int}}$ as a function of time (Fig. 4.2). I modified the one-dimensional diffusion model of Demouchy and Mackwell (14) according to the procedure of Shewmon (67) to vary the equilibrium H-concentration to desired values. In this model, the concentration ($C_{X,t}$) at a given point (X) in a crystal of width h = 0.002 m (2 mm) is a function of time (t), initial concentration (C_0), imposed equilibrium concentration (C_{eq}), and the diffusion coefficient (D, as calculated from equations 4.2 and 4.3):

$$C_{X,t} = \left(C_{eq} - C_0\right) \cdot \left\{\left[erfc\left(\frac{X}{2\sqrt{Dt}}\right)\right] + \left[erfc\left(\frac{X-h}{2\sqrt{Dt}}\right)\right]\right\} + C_0, \quad (4.5)$$

where *erfc* represents the complementary error function. I then calculated $r_{A_{int}}$ from the diffusion profiles using Equation 4.4. I processed all calculations using Microsoft Excel ©. Unlike the anhydrous model (above), these diffusion models produce unrealistic results at extended times. Thus, I included results from the anhydrous model in Figure 4.2 to show that the models agree with one another for the durations considered here.

Figure 4.2 shows the results of these calculations at C_{eq} ranging from 0 to 5/4 of an arbitrary starting concentration (C_0) of 100 ppm[1], for a temperature of 1100 °C. The curves illustrate that the rate at which $r_{A_{int}}$ decreases depends on the equilibrium H concentration imposed by the surrounding environment. In the anhydrous equilibrium condition (equivalent to Figure 4.1), $r_{A_{int}}$ declines to 0.46 after 20 min, whereas the ratio reaches 0.73 if the surrounding environment imposes a H concentration equal to half the starting concentration, for the *c* axis. Unsurprisingly, $r_{A_{int}}$ remains at unity indefinitely if the olivine remains in equilibrium with its surroundings, and begins to increase where the equilibrium concentration exceeds the initial concentration. Because the value of C_{eq} should be a function of the activity of water dissolved in magma (11, 23), these models suggest that elevated magmatic water concentrations limited diffusive loss of H from xenolith and macrocrystic olivines from Jericho and Beartooth. However, estimation of magmatic water concentration from comparison of diffusion models with natural data is not possible at present, because activity coefficients for kimberlite magmas are unavailable. Furthermore, C_{eq} also depends on the fugacity of water (15, 16), which is

[1]At a given time and temperature, the ratio $r_{A_{int}}$ is a function of the ratio of the initial H concentration (C_0) to the imposed equilibrium concentration (C_{eq}). Thus, the labels in Figure 4.2 show C_{eq} as a function of C_0, as opposed to absolute values. Nevertheless, a C_0 of 100 ppm is a reasonable value because kimberlitic olivines commonly have H-concentrations on that order.

pressure dependent, indicating that C_{eq} probably continuously decreases during

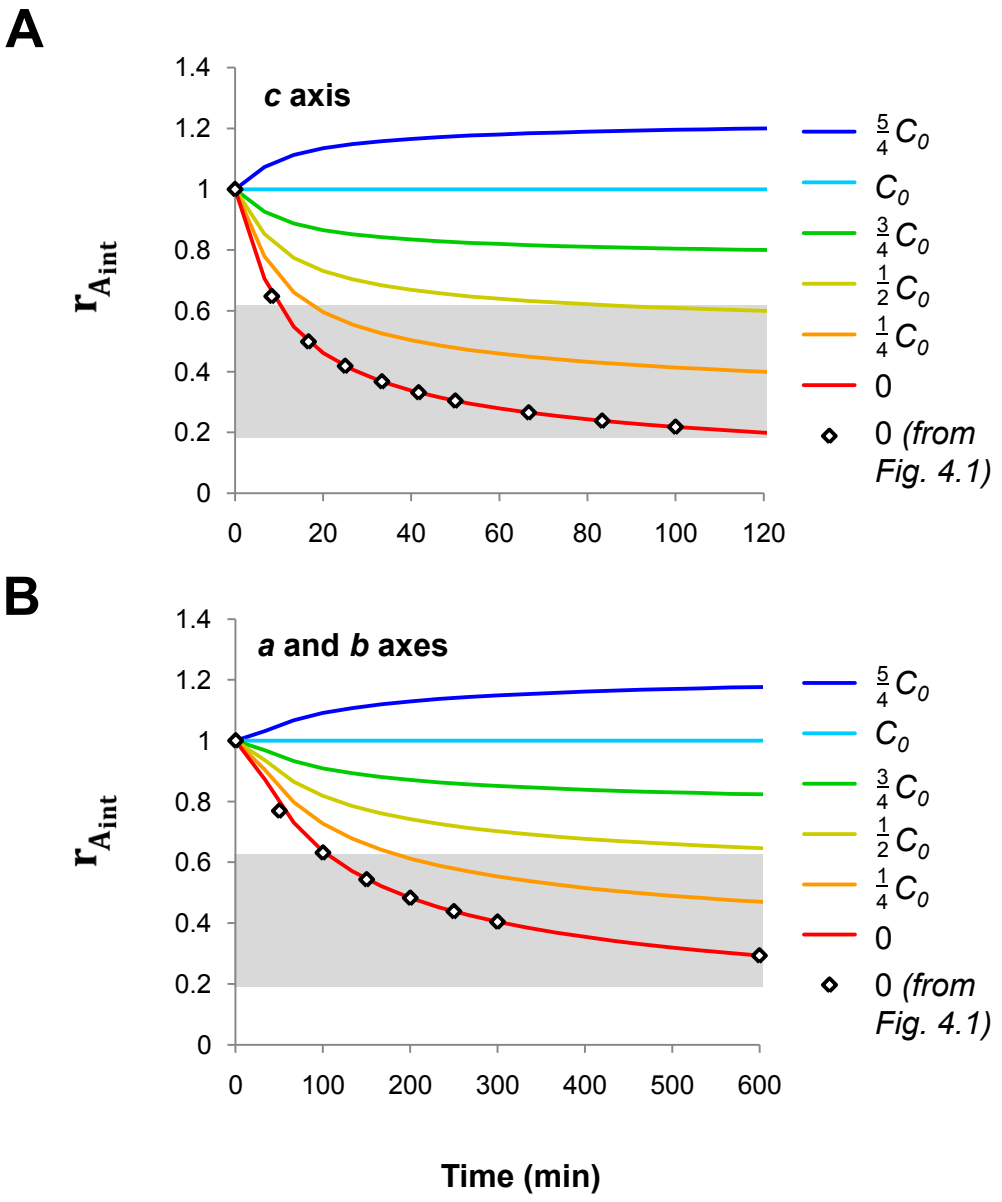

Figure 4.2: Diffusive changes in H-zonation in olivine as a function of imposed equilibrium H-concentration, time, and crystallographic direction, for H-bearing olivine re-equilibrating at 1100 °C. The *y* axis shows the rim:core intensity ratio, $r_{A_{int}}$. The imposed equilibrium concentration for each curve appears at the right, relative to the initial concentration (C_0). *Diamond-shaped symbols* represent the model used in Figure 4.1. The *shaded region* represents the range of values from Matsoku and Pipe 200 olivines. (**A**) Zonation resulting from diffusion along the *c* axis. (**B**) Zonation resulting from diffusion along the *a* and *b* axes.

decompression (13). Thus, although the contrasting $r_{A_{int}}$ values measured in olivines from the southern African (Matsoku, Pipe 200) and Lac de Gras (Jericho, Beartooth) kimberlites could indicate greater enrichment of water in the latter, the specific magmatic water concentrations remain unclear. Finally, in consideration of figures 4.1 *and* 4.2, either different thermal histories and/or magmatic water concentrations could explain the locality-specific $r_{A_{int}}$. Duration of diffusion (*i.e.*, ascent time) critically affects zonation in either regime.

4.3.3 Other Factors that Affect H-Zonation

Abrasion, resorption, or alteration of olivine during or following emplacement can modify zonation profiles that develop by diffusion. The cores of macrocrysts are commonly rounded, indicating that these crystals (whether xenocrysts or phenocrysts) experienced resorption (2, 32) or abrasion (19, 26) during transport, before crystallization of late rims. These erosive processes compete with the development of diffusive zonation profiles. If the rate of olivine removal exceeds the rate of diffusion, no detectable zoning profile develops. In less severe cases, slower olivine removal narrows the diffusion profile, in comparison to the case of no removal. These effects appear to have contributed little to zoning trends, because zoning is at least as prevalent in the macrocrysts as it is in the xenolith olivines, which are protected from such processes. However, future studies may disprove this argument, because the small number of xenolith and macrocryst samples investigated may not be representative.

In Section 4.2, I argued that alteration does not influence previously developed H-diffusion patterns. However, alteration may disturb zoning trends if pseudomorphs partially replace the margins of olivines (*e.g.*, Fig. 3.4 C); this form of replacement obscures the original grain boundary, and thus could result in incorrect placement of 'rim' analyses that could lead to unrepresentative $r_{A_{int}}$ values. The extent of this replacement varies among different kimberlites (and among different crystals in individual intrusions) (2), and was not easy to observe using the FTIR microscope. In general, the Jericho macrocrysts are well preserved (the pseudomorphs do not fully replace the thin overgrowth rims), and no serpentine is associated with the Beartooth olivines. The degree of alteration of the Pipe 200 macrocrysts is less obvious, because no normal thin sections of this kimberlite were manufactured. However, the evident zonation

of the infrared peaks in the larger macrocrysts indicates that these olivines are sufficiently well preserved to permit analysis of their H-zonation. Pseudomorphs are not extensive in the xenolith olivines, as evinced by the typical thinness of intergranular serpentine; alteration affects some olivines in sample 53 from Jericho more substantially, but others from the sample are fresh, and also show little H-zonation. Thus, the effects of pseudomorphs on zonation relationships appear to be minimal.

4.3.4 Possible Causes of Intrusion-Specific H-Zonation

The diffusion models presented in figures 4.1 and 4.2 permit a semi-quantitative interpretation of measured $r_{A_{int}}$ values. Crystals from Pipe 200 and Matsoku have minimum $r_{A_{int}}$ of ~0.2. Additionally, spectra from xenolith olivine rims and macrocrysts (Pipe 200 only) were typically near the detection limit of the FTIR setup (previously estimated at 1 ppm H_2O (11), probably ~5-10 ppm here because of the smaller beam). Figure 4.2 shows that, for an olivine crystal to exhibit $r_{A_{int}}$ of this value, it must exist in a water-poor environment. Thus, the low $r_{A_{int}}$ and nearly anhydrous rims of these olivines necessitate that they experienced low water activities at sufficiently high temperatures to permit development of H diffusion profiles. In contrast, typical $r_{A_{int}}$ values (~0.9) of Jericho and Beartooth olivines suggest comparatively high water activities, as these values could not be maintained under high temperatures for any appreciable length of time in an anhydrous environment.

The weak zonation of the Jericho and Beartooth olivines indicates that these olivines travelled in cooler magmas, experienced higher water activities, or ascended more rapidly than the Matsoku and Pipe 200 samples. Throughout most of the ascent of kimberlite magma, temperature decreases theoretically result from decompression (adiabatic temperature change), heat transfer to entrained xenoliths, and heat consumed by xenocryst assimilation (5). However, the factor that could more dramatically affect the thermal evolution of ascending kimberlite magma is the amount and exsolution of water (Fig. 4.3) (5). Kavanagh and Sparks (5) predicted (using a thermodynamic model that incorporates the effects of lithospheric contamination, xenocryst assimilation, and crystallization) that water-rich (10 wt. % H_2O) magma ascending from a depth of 200 km initially cools more rapidly than water-poor (5 wt. % H_2O) magma. Exsolution of fluid triggers crystallization of olivine, causing the release of latent heat and effectively

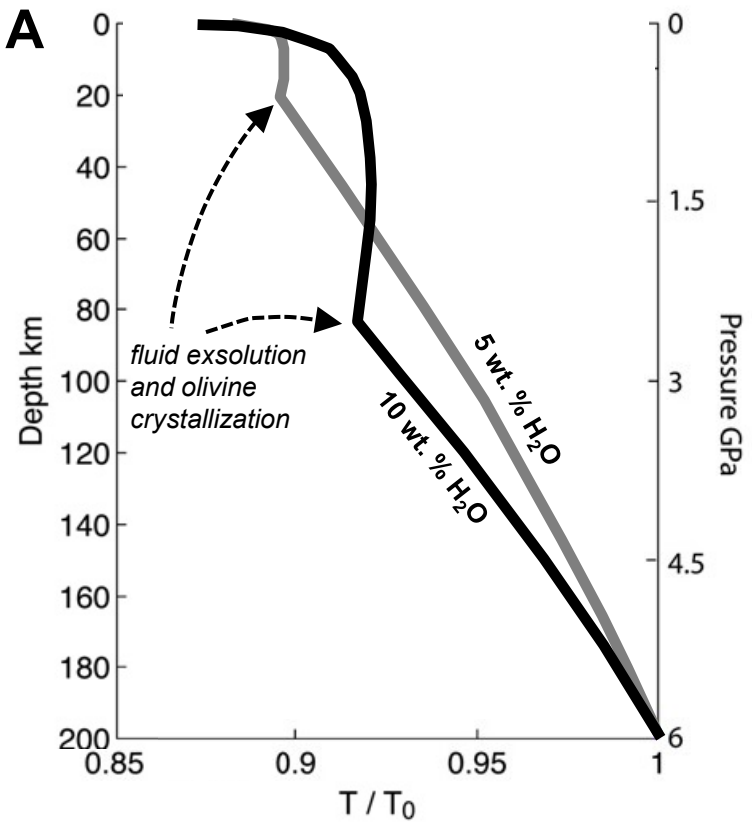

Figure 4.3: Temperature *v.* depth models for 5 wt. % H_2O and 10 wt. % H_2O kimberlite magmas. The content of magmatic water significantly changes the evolution of temperature during ascent, as well as the depth of fluid exsolution and consequent olivine crystallization, thereby providing two mechanisms by which water concentration could affect diffusion of H in olivine. The *x* axis shows temperature as the ratio of temperature *T* to initial temperature T_0. After Kavanagh and Sparks (5).

counteracting adiabatic cooling until shallow depths. This crystallization begins at ~80 km depth for the water-rich magma, and ~20 km depth for the water-poor magma (Fig. 4.3). Magmas with 5 wt. % water remain hotter than those with 10 wt. % water for the initial 140 km of ascent, whereas the latter becomes hotter for most of the remaining distance, at the same initial temperature. Thus, variable water concentrations produce differing cooling paths that could influence the extent of diffusive H loss experienced by olivine. Unfortunately, the H-diffusion models in figures 4.1 and 4.2 are not suited to confirm whether the water-poor temperature pathway would encourage more diffusive H-exchange between magma and olivine. Elucidation of these relationships requires diffusion models that allow continuous variation of temperature. Another point of caution is that the effect of water concentration is significantly different when considered in isolation from assimilation, contamination, and crystallization (5). Thus, many factors could accentuate or minimize the influence of water on the thermal evolution of kimberlite magma.

The thermodynamic models of Kavanagh and Sparks (5) also illustrate how different water concentrations could produce striking differences in the evolution of the activity (or fugacity) of water during magma ascent. If their solubility models reasonably approximate the depth of fluid exsolution, magmas with 10 wt. % H_2O could exsolve fluid at ~80 to ~120 km depth (depending on CO_2 content), at least 60 km deeper than magma with 5 wt. % H_2O (exsolution at ~20 km depth) (Fig. 4.3). If fluid remains coupled to the magma, the water-rich system should experience a dramatic increase in the activity of water upon exsolution for a longer duration than the predominantly water-undersaturated ascent of the water-poor magma. The water-rich magma would thereby limit diffusive H-loss from olivine, owing to higher activity/fugacity of water over longer durations. In addition, the water-saturated magma would undoubtedly ascend more rapidly than an equivalent magma that continually loses fluid to the country rocks, owing to the low viscosity and density of aqueous fluid. That is, water-enrichment could reduce the duration of H-diffusion at high temperature. Thus, different primary (*i.e.*, initial) magmatic water concentrations could explain the differing H-zonation patterns. Kopylova *et al*. (69) estimated that the parental Jericho magma contained ~9 wt. % of water, close to the 10 % model of Kavanagh and Sparks (5). This estimate may be an underestimate

because the quenched kimberlite analyzed contains abundant vesicles, indicative of degassing (69). Thus, early, deep exsolution of magmatic water may have influenced H diffusion in Jericho olivines in a manner consistent with Figure 4.3 (5). How this water concentration compares to the Beartooth, Pipe 200, and Matsoku magmas remains unclear, owing to the lack of comparable magma composition estimates for these intrusions.

Alternatively, all the kimberlites examined in this study could have had identical initial magma compositions, if exsolved fluids continually escaped from the magma to the country rocks following initial exsolution. Fedortchouk *et al*. (8) postulated that the variable resorption morphologies of diamonds among Lac de Gras kimberlites resulted from different depths of fluid escape following exsolution. In this regard, the Pipe 200 and Matsoku magmas could have lost fluid to the country rocks at a relatively early stage, thereby reducing the activity of water in the system, and encouraging loss of H from olivine.

Above, I argued that the limited extent of H-zonation in Jericho and Beartooth olivines suggests high magmatic water concentrations in comparison to Pipe 200 and Matsoku. This argument is problematic because olivine in kimberlites spans a wide range of H concentrations (*e.g.*, 0 to ~550 ppm H_2O for Beartooth olivines (8)); presumably some of these olivines have H concentrations above the value imposed by the surrounding magma, and some have more H-poor compositions. If true, then the H-rich olivines should have normal zoning (H-loss, $r_{A_{int}} < 1$), whereas H-poor olivines should have reverse zoning (H-grain, $r_{A_{int}} > 1$), and the ratio $r_{A_{int}}$ should be more extreme for olivines that deviate greatly from the equilibrium concentration; that is, crystals corresponding to multiple curves in Figure 4.2 should be present. In Figure 3.9 (A and C), few to no crystals show increases in rim H concentration that lie outside of estimated uncertainties, whereas decreases commonly extend beyond uncertainties. I speculate that this phenomenon results from continuous variation in the equilibrium H concentration, which results in part from the effects of decompression on water fugacity (15, 16), and in part from changes in water activity/fugacity that accompany fluid exsolution. Because decreasing water fugacity decreases the H solubility in olivine (15, 16), crystals of all H concentrations experience some degree of H loss during the low pressure phase of

emplacement. I expect that a combination of this effect, and rapid ascent times of the Jericho and Beartooth magmas, tended to produce weak H-loss in the margins of the crystals. This interpretation is overly complex to be supported or rejected by the simple diffusion models in Figure 4.2, because those models have fixed equilibrium conditions; models that can vary the equilibrium conditions could test the viability of this hypothesis.

An alternative interpretation of weak zoning is that the crystals completely re-equilibrated with, or directly crystallized from the magma. Matveev and Stachel (11), and Fedortchouk *et al*. (8) proposed these interpretations on the basis of their assignment of equilibrium pressures to olivines with different spectrum types. The validity of these interpretations depends on whether spectrum type is a reliable semi-quantitative barometer (Section 1.3.2), whether kimberlite magmas commonly stagnate at depth, and whether they crystallize abundant coarse-grained olivine. Under either interpretation, kimberlites containing weakly zoned, H-bearing olivine cannot have been essentially anhydrous, as Kamenetsky *et al*. (19) advocated for the Udachnaya-East kimberlite, unless the ascent duration experienced by typical xenocrysts is shorter than ~20 min. Indeed, Udachnaya-East itself must have been enriched in water, given the elevated H concentrations in its olivines (19) (many > 300 ppm H_2O, if corrected to the calibration of Bell *et al*. (37)). However, kimberlites with strongly H-depleted olivines could have low water concentrations for much of their ascent, if we accept the fast ascent durations required to produce the zonation of Matsoku and Pipe 200 olivines under anhydrous conditions (Fig. 4.1).

In summary, a combination of different magmatic thermal histories, water contents, or ascent durations could result in contrasting diffusive H-zonation patterns. None of these three variables is likely to vary in isolation; temperature evolves differently as a function of volatile contents (5), as should magma ascent rates. The variable that I believe is most likely to produce the variations is magmatic water content, because it demonstrably varies among different kimberlites (8), and can theoretically influence both thermal history (5) and ascent duration. Furthermore, different densities and viscosities of aqueous fluid and magma could allow water to separate from magma, thereby providing a physical mechanism that could produce variable volatile concentrations. I speculate that elevated water concentrations in Beartooth and Jericho magmas caused rapid, possibly

cooler ascent that restricted the degree of H diffusion in comparison with Matsoku and Pipe 200 magmas. These latter two magmas may have lost aqueous fluid during ascent, or had initially water-poor compositions.

4.3.4 Group 1 H-Zonation: A Possible Proxy for Diamond Grade

Figure 3.9 (D, E) shows the degree of H-zonation for olivines hosted in diamondiferous (Jericho, Beartooth) and diamond-poor (Matsoku, Pipe 200) kimberlites. Olivines from diamond-poor kimberlites define a distinct, H-depleted zonation pattern in comparison to the restricted zonation of the other olivines. These results suggest that H-zonation in olivine may be a useful proxy for diamond grade, although this finding is tentative owing to the small sample size. The origin of this correlation may result from any of the factors that affect H-diffusion (Section 4.3.3). Hotter temperatures would favour H-diffusion in olivine and resorption/graphitization of diamond. Slower ascent of water-poor magmas could increase the time of resorption and graphitization reactions (8).

The correlation between H-zonation in olivine and diamond grade is variably supported by other studies. Among the six diamondiferous kimberlites examined to date (17, 48, 52), only the Finsch kimberlite contains H-depleted xenolith olivines. Of the two diamond-poor kimberlites (Thaba Putsoa and Matsoku, Lesotho) analyzed by other researchers (48), neither of the two xenoliths are detectably zoned with respect to H. This result is surprising in light of the strong zonation of H in the Matsoku xenolith reported here; clearly, analysis of multiple xenoliths from the same intrusion is essential to elucidate the typical or representative zonation trend. Intra-locality variability could significantly modify the conclusions of this work.

Another drawback to this study is the sampling strategy. Future studies would ideally link the *context* of the sample (*e.g.*, lithofacies of host kimberlite, relative sequence of host magma pulse) to the diffusion profiles. This point could be significant from an economic standpoint, because different phases of kimberlite intrusion may have distinct diamond grades. For example, Pipe 200 is predominantly a barren kimberlite, but one of its three phases is diamondiferous (56). Similarly, different magma pulses may have contrasting volatile contents, and thus exert their own influences on the H-zonation patterns of their olivines, which may or may not correlate with the diamond grade of individual magma pulses.

The inconsistencies among published data and my results indicate that application of H-zonation as a proxy for diamond grade is preliminary. However, the small number of samples in total is insufficient to rule out the usefulness of such an application. I recommend that a larger study devoted to this topic be undertaken prior to any practical application; such a study should examine xenolith and macrocrystic olivines from many kimberlites of known diamond grade to determine the strength of the correlation between H zonation in olivine and diamond abundance. If this correlation is reliable, it may prove invaluable to the diamond industry. In contrast to indicator mineral compositions (70, 71), which reflect the diamond potential of the mantle sampled by an intrusion, H zonation in olivine is a proxy for *ascent* processes, and therefore could reflect the degree of diamond *preservation*.

4.4 Defect-Specific Diffusion

Figures 3.5, 3.8, 3.10, and 3.11 illustrate that different peaks in the infrared spectrum experience differing degrees of attenuation in the rims of zoned olivines; for example, Figure 3.11 shows that Group 2 peaks generally attenuate more strongly than Group 1 peaks in the rims of Beartooth olivines. Furthermore, Group 1 and Group 2 peaks appear to be independently zoned; in Figure 3.10, zonation of Group 1 and Group 2 peaks typically correlates, but in several Group 1B type crystals, zonation in one group is completely independent of the other (vertical and horizontal core-rim pairs). These phenomena imply that different H defects in olivine can diffuse independently. Although different peak attenuations also exist within Group 1 region itself, I focus here on comparison between Group 1 and Group 2 peaks, given the apparent importance of the latter as proxies for diamond quality and magmatic volatile saturation (8). However, defect-specific diffusion within the Group 1 region is probably an important phenomenon for the mechanisms of H diffusion in olivine. These matters are beyond the scope of this work and I do not discuss them further.

In general, Group 2 H attenuates more strongly than Group 1 H in Beartooth olivines (Fig. 3.11); the average $r_{A_{int}}$ for Group 1 peaks (0.9) is greater than that of Group 2 peaks (0.75). One explanation for this phenomenon is that Group 2 H defects diffuse more rapidly than most Group 1 H defects, resulting in greater Group 2

attenuation. If this explanation is correct, previous estimates of xenolith ascent duration based on H diffusion in olivine (17, 50, 55) have underestimated the duration. These studies applied the diffusion coefficients of Demouchy and Mackwell (14), which these authors estimated from experiments on Group 2-dominated olivines, to olivines dominated by Group 1 H. Thus, if diffusion of Group 2 H defects is faster than Group 1 H, the ascent duration estimates must be too short. Similarly, quantitative application of the models in figures 4.1 and 4.2 to diffusion in Group 1-dominated olivine would produce short time estimates. However, factors other than differing diffusion coefficients could explain the preferential attenuation of Group 2 peaks.

Preferential attenuation of Group 2 peaks could result from the chemical environment in kimberlite magmas. Specifically, kimberlite magmas have silica activities well below the forsterite-orthopyroxene buffer (25, 72); if high silica activity is important for stabilizing Group 2 defects, as is generally supported by experimental studies (14, 40, 42, 46, 49), the equilibrium concentration of these defects may be close to zero for the whole ascent period. In contrast, Group 1 defects stabilized by Ti-related defects (42) or Si vacancies (40, 41) could have equilibrium concentrations above zero for much of the ascent, owing to the high Ti concentrations (1, 73) and low silica activities (25, 72), respectively, in kimberlite magmas. Thus, even if the diffusion coefficient is the same, different equilibrium concentrations for Group 1 and Group 2 defects may produce variable $r_{A_{int}}$values within single crystals, which necessarily experience a single thermal history. That is, Group 1 defects may behave similarly to the curves in Figure 4.2 that represent equilibrium concentrations greater than zero, whereas Group 2 peaks may fall along the 'anhydrous olivine' curve throughout ascent (Figure 4.1). This interpretation implies that the Si vacancy structure can rearrange at a similar pace to H diffusion. However, the diffusion coefficient for Si in H-bearing olivine (74) is orders of magnitude smaller than that of H, suggesting that this mechanism of preferential Group 2 H-loss is unlikely important on short timescales. Resetting of the trivalent cation structure could also encourage Group 2 H-loss; unfortunately, diffusion coefficients of trivalent cations in H-bearing olivine are unavailable for comparison.

The independent zoning behaviour of Group 1 and Group 2 H defects in some olivines (Fig. 3.10) cannot be explained by differing diffusion rates alone. These

behaviours could represent contrasting dependences of diffusion on crystallographic direction for Group 1 and Group 2 peaks. However, this option is unattractive because authors of diffusion studies reported no such differential anisotropy (14). Another possibility is that contrasting chemical environments (*e.g.*, oxygen fugacities, trivalent cation content) around these crystals favoured diffusion of one H defect type over the other. However, this mechanism seems unlikely, because it requires that different crystals reside in stable chemical environments for extended periods of time; this requirement seems incompatible with the vigorous mixing of heterogeneous materials that probably typifies ascent of kimberlite magmas. Thus, the reason for independent zonation of Group 1 and Group 2 H remains unclear.

Regardless of the mechanism responsible for differential Group 2 attenuation, the phenomenon itself may explain the distribution of Group 2-bearing olivines in Lac de Gras kimberlites. These olivines are restricted to kimberlites dominated by volcaniclastic facies, which contain diamonds that appear to have been resorbed by magmatic aqueous fluid (8). Fedortchouk *et al*. (8) reasoned that this correlation indicates a previously unrecognized dependence of Group 2 defects on water saturation, assuming that the olivines were in equilibrium with their host magma. In light of the preferential loss of Group 2 peaks discovered here, and the possibility that these olivines may not represent magmatic equilibrium, I propose an alternative explanation for their distribution in Lac de Gras kimberlites; the association of Group 2-bearing olivines and water-resorbed diamonds may result from superior preservation of mantle-derived H defects in rapidly ascending, water-saturated magmas. In the kimberlites dominated by hypabyssal facies, which lack Group 2-bearing olivines (8), Group 2 H may have completely diffused out of the olivines during a slower ascent in water-undersaturated melts. If this explanation is correct, Group 2 bands in olivine may reflect diamond quality only in kimberlites that passed through regions of the mantle that contained Group 2-bearing olivines. Whether such olivines are present in portions of most cratonic mantle roots remains to be elucidated.

4.5 Summary and Future Directions

The first goal of this study was to determine whether xenolith olivines in contact with kimberlite magmas gain or lose H, and whether Group 2 peaks intensify or attenuate near

the kimberlite. None of xenolith samples exhibits any special zonation trend in olivines in contact with kimberlite; olivines in the cores of xenoliths have the same zonation trends as those in the rims, in contradiction to my initial hypothesis. The olivines that have significant zonation show depletion of H in their rims. None of the xenolith olivines contained Group 2 peaks, so the behaviour of these defects in xenolith olivines remains unclear.

The second goal of this study was to compare zonation of macrocrysts to xenolith olivines to determine whether macrocrysts better equilibrate than xenolith olivines. Xenolith and macrocryst olivines from the same kimberlite appear to share common H-zonation trends, with no evident preferential zonation of macrocrysts. Group 2 H defects typically deplete more readily in rims of macrocrysts (Beartooth olivines only).

The most significant finding of this study is the apparent locality-specific H-zonation style of kimberlitic olivine. Olivines from Beartooth and Jericho kimberlites show limited zonation, whereas the Matsoku and Pipe 200 olivines show significant H depletion. This finding shows that significant variation in one or more of the following factors that influence diffusion of H in olivine must exist among different localities: thermal history, water activity, and ascent rate. I believe variation in magmatic water concentration is the most likely cause of differing zonation patterns, and that the control magmatic water exerts on the thermal evolution and ascent rate of magma significantly affects the extent of diffusion. These factors are all important for reconstructing the petrogenesis of kimberlite magmas, and each can contribute to the preservation of diamonds during transport. Future investigators could compare estimates of temperature (*e.g.*, from olivine-ilmenite thermometry (29, 75)) and magma ascent duration (*e.g.*, from Ar loss in phlogopite (6, 68), garnet reaction rims (66)) to zonation patterns from these (or other) kimberlites to better elucidate which of these factors may have contributed to the variability.

The conditions that produce different H zonation patterns could influence the diamond grade of kimberlites; the intrusions with strongly zoned crystals are diamond-poor, whereas the others are rich in diamond. However, some inconsistencies among my findings and those of previous studies (48, 52) require that the correlation between H zonation in olivine and diamond grade be tested in a larger study prior to application. I

suggest comparing the degree of H-loss in olivine from xenoliths (multiple samples per intrusion) and the macrocryst population in a number of kimberlites that span a range of known diamond grades. This type of investigation could conclusively determine whether H-zonation in olivine is a suitable proxy for the preservation of diamonds in kimberlites, if combined with compositional studies of indicator minerals (70) (which should elucidate whether the mantle sampled was likely diamondiferous at the time of kimberlite magmatism). One could perform this study on both regional and global scales to determine whether H-zonation phenomena are suitable for identifying the most promising kimberlites within a related cluster of intrusions, and/or predicting the diamond grade of specific phases within individual intrusions.

In some cases, specific H defects are differentially zoned within individual crystals. Group 2 peaks generally attenuate more profoundly than Group 1 peaks in olivine rims, possibly owing to differential diffusion rates of Group 1 and Group 2 H defects. One could test this hypothesis by annealing Group 2- and Group 1-bearing olivines in identical environments to elucidate whether these defects diffuse independently. Significant consequences of defect-specific diffusion coefficients could include: corrections to previous ascent rate estimates (17, 50, 55), and revised models of cation diffusion mechanisms, which are linked to the rheological properties of mantle rocks (13, 74). Regardless of its cause, preferential loss of Group 2 H suggests that the absence of these olivines in water-undersaturated, hypabyssal facies-dominated kimberlites (8) results from the preferential loss of Group 2 H during a relatively prolonged ascent, as compared with otherwise equivalent, water-saturated, volcaniclastic intrusions. Future researchers could test this hypothesis by comparing the ascent rates of intrusions that contain Group 2-bearing olivines with those that do not, preferably within a related cluster of kimberlites, such as the Lac de Gras intrusions.

REFERENCES

1. Mitchell, R. H. 2008. Petrology of hypabyssal kimberlites: Relevance to primary magma compositions. *Journal of Volcanology and Geothermal Research* 174:1-8.
2. Mitchell, R. H. 1986. *Kimberlites: Mineralogy, Geochemistry, and Petrology*. Plenum Press, New York.
3. Sparks, R. S. J., R. A. Brooker, M. Field, J. Kavanagh, J. C. Schumacher, M. J. Walter, and J. White. 2009. The nature of erupting kimberlite melts. *Lithos* 112:429-438.
4. Sparks, R. S. J., L. Baker, R. J. Brown, M. Field, J. Schumacher, G. Stripp, and A. Walters. 2006. Dynamical constraints on kimberlite volcanism. *Journal of Volcanology and Geothermal Research* 155:18-48.
5. Kavanagh, J. L., and R. S. J. Sparks. 2009. Temperature changes in ascending kimberlite magma. *Earth and Planetary Science Letters* 286:404-413.
6. Wartho, J. A., and S. P. Kelley. 2003. Ar-40/Ar-39 ages in mantle xenolith phlogopites: determining the ages of multiple lithospheric mantle events and diatreme ascent rates in southern Africa and Malaita, Solomon Islands. In *Geochronology: Linking the Isotopic Record with Petrology and Textures*, London. 231-248.
7. Mercier, J. C. C. 1979. Peridotite xenoliths and the dynamics of kimberlite intrusion. In *The Mantle Sample: Inclusions in Kimberlites and Other Volcanics*. F. R. Boyd, and H. O. A. Meyer, eds. American Geophysical Union, Washington. 197-212.
8. Fedortchouk, Y., S. Matveev, and J. A. Carlson. 2010. H_2O and CO_2 in kimberlitic fluid as recorded by diamonds and olivines in several Ekati Diamond Mine kimberlites, Northwest Territories, Canada. *Earth and Planetary Science Letters* 289:549-559.
9. Fedortchouk, Y., D. Canil, and E. Semenets. 2007. Mechanisms of diamond oxidation and their hearing on the fluid composition in kimberlite magmas. *American Mineralogist* 92:1200-1212.
10. Arima, M., and Y. Kozai. 2008. Diamond dissolution rates in kimberlitic melts at 1300-1500 °C in the graphite stability field. *European Journal of Mineralogy* 20:357-364.
11. Matveev, S., and T. Stachel. 2007. FTIR spectroscopy of OH in olivine: A new tool in kimberlite exploration. *Geochimica Et Cosmochimica Acta* 71:5528-5543.
12. Matveev, S., and T. Stachel. 2009. Evaluation of kimberlite diamond potential using FTIR spectroscopy of xenocrystic olivine. *Lithos* 112:36-40.
13. Mackwell, S. J., and D. L. Kohlstedt. 1990. Diffusion of hydrogen in olivine - implications for water in the mantle. *Journal of Geophysical Research-Solid Earth and Planets* 95:5079-5088.
14. Demouchy, S., and S. Mackwell. 2006. Mechanisms of hydrogen incorporation and diffusion in iron-bearing olivine. *Physics and Chemistry of Minerals* 33:347-355.
15. Kohlstedt, D. L., H. Keppler, and D. C. Rubie. 1996. Solubility of water in the alpha, beta and gamma phases of $(Mg,Fe)_2SiO_4$. *Contributions to Mineralogy and Petrology* 123:345-357.

16. Bai, Q., and D. L. Kohlstedt. 1992. Substantial hydrogen solubility in olivine and implications for water storage in the mantle. *Nature* 357:672-674.
17. Peslier, A. H., A. B. Woodland, and J. A. Wolff. 2008. Fast kimberlite ascent rates estimated from hydrogen diffusion profiles in xenolithic mantle olivines from southern Africa. *Geochimica Et Cosmochimica Acta* 72:2711-2722.
18. Brett, R. C., J. K. Russell, and S. Moss. 2009. Origin of olivine in kimberlite: Phenocryst or impostor? *Lithos* 112:201-212.
19. Kamenetsky, V. S., M. B. Kamenetsky, A. V. Sobolev, A. V. Golovin, S. Demouchy, K. Faure, V. V. Sharygin, and D. V. Kuzmin. 2008. Olivine in the Udachnaya-East kimberlite (Yakutia, Russia): Types, compositions and origins. *Journal of Petrology* 49:823-839.
20. Kopylova, M. G., G. M. Nowell, D. G. Pearson, and G. Markovic. 2009. Crystallization of megacrysts from protokimberlitic fluids: Geochemical evidence from high-Cr megacrysts in the Jericho kimberlite. *Lithos* 112:284-295.
21. Gurney, J., W. R. O. Jakob, and J. B. Dawson. 1979. Megacrysts from the Monastery Kimberlite Pipe, South Africa. In *The Mantle Sample: Inclusions in Kimberlites and Other Volcanics*. F. R. Boyd, and H. O. A. Meyer, eds. American Geophysical Union, Washington. 227-243.
22. Eggler, D. H., M. E. McCallum, and C. B. Smith. 1979. Megacryst assemblages in kimberlites from northern Colorado and southern Wyoming: Petrology, geothermometry-barometry, and areal distribution. In *The Mantle Sample: Inclusions in Kimberlites and Other Volcanics*. F. R. Boyd, and H. O. A. Meyer, eds. American Geophysical Union, Washington. 213-226.
23. Bell, D. R., G. R. Rossman, and R. O. Moore. 2004. Abundance and partitioning of OH in a high-pressure magmatic system: Megacrysts from the Monastery kimberlite, South Africa. *Journal of Petrology* 45:1539-1564.
24. Davies, G. R., A. J. Spriggs, and P. H. Nixon. 2001. A non-cognate origin for the Gibeon kimberlite megacryst suite, Namibia: Implications for the origin of Namibian kimberlites. *Journal of Petrology* 42:159-172.
25. Mitchell, R. H. 1973. Composition of olivine, silica activity and oxygen fugacity in kimberlite. *Lithos* 6:65-81.
26. Arndt, N. T., M. Guitreau, A. M. Boullier, A. Le Roex, A. Tommasi, P. Cordier, and A. Sobolev. 2010. Olivine, and the origin of kimberlite. *Journal of Petrology* 51:573-602.
27. Francis, D., and M. Patterson. 2008. Kimberlites and aillikites as probes of the continental lithospheric mantle. *Lithos* in press.
28. Patterson, M., D. Francis, and T. McCandless. 2009. Kimberlites: Magmas or mixtures? *Lithos* 112:191-200.
29. Fedortchouk, Y., and D. Canil. 2004. Intensive variables in kimberlite magmas, Lac de Gras, Canada and implications for diamond survival. *Journal of Petrology* 45:1725-1745.
30. Hunter, R. H., and L. A. Taylor. 1984. Magma-mixing in the low velocity zone: kimberlitic megacrysts from Fayette County, Pennsylvania. *American Mineralogist* 69:16-29.

31. Boyd, F. R., and C. R. Clement. 1977. Compositional zoning of olivine in kimberlite from the De Beers Mine, Kimberly, South Africa. In *Carnegie Institute of Washington Yearbook*, Washington. 485-493.
32. Nielsen, T. F. D., and K. K. Sand. 2008. The Majuagaa kimberlite dike, Maniitsoq region, West Greenland: Constraints on an Mg-rich silicocarbonatitic melt composition from groundmass mineralogy and bulk compositions. *Canadian Mineralogist* 46:1043-1061.
33. Miller, G. H., G. R. Rossman, and G. E. Harlow. 1987. The natural occurrence of hydroxide in olivine. *Physics and Chemistry of Minerals* 14:461-472.
34. Matsyuk, S. S., and K. Langer. 2004. Hydroxyl in olivines from mantle xenoliths in kimberlites of the Siberian platform. *Contributions to Mineralogy and Petrology* 147:413-437.
35. Khisina, N. R., R. Wirth, M. Andrut, and A. V. Ukhanov. 2001. Extrinsic and intrinsic mode of hydrogen occurrence in natural olivines: FTIR and TEM investigation. *Physics and Chemistry of Minerals* 28:291-301.
36. Stuart, B. H. 2004. *Infrared Spectroscopy: Fundamentals and Applications*. John Wiley and Sons, Ltd., West Sussex.
37. Bell, D. R., G. R. Rossman, J. Maldener, D. Endisch, and F. Rauch. 2003. Hydroxide in olivine: A quantitative determination of the absolute amount and calibration of the IR spectrum. *Journal of Geophysical Research-Solid Earth* ECV8:1-ECV8-2.
38. Beran, A., and A. Putnis. 1983. A model of the OH positions in olivine, derived from infrared-spectroscopic investigations. *Physics and Chemistry of Minerals* 9:57-60.
39. Bell, D. R., and G. R. Rossman. 1992. Water in Earth's mantle - the role of nominally anhydrous minerals. *Science* 255:1391-1397.
40. Matveev, S., H. S. O'Neill, C. Ballhaus, W. R. Taylor, and D. H. Green. 2001. Effect of silica activity on OH-IR spectra of olivine: Implications for low-aSiO_2 mantle metasomatism. *Journal of Petrology* 42:721-729.
41. Lemaire, C., S. C. Kohn, and R. A. Brooker. 2004. The effect of silica activity on the incorporation mechanisms of water in synthetic forsterite: a polarised infrared spectroscopic study. *Contributions to Mineralogy and Petrology* 147:48-57.
42. Berry, A. J., J. Hermann, H. S. C. O'Neill, and G. J. Foran. 2005. Fingerprinting the water site in mantle olivine. *Geology* 33:869-872.
43. Walker, A. M., J. Hermann, A. J. Berry, and H. S. O'Neill. 2007. Three water sites in upper mantle olivine and the role of titanium in the water weakening mechanism. *Journal of Geophysical Research-Solid Earth* 112:-.
44. Berry, A. J., H. S. C. O'Neill, J. Hermann, and D. R. Scott. 2007. The infrared signature of water associated with trivalent cations in olivine. *Earth and Planetary Science Letters* 261:134-142.
45. Bai, Q., and D. L. Kohlstedt. 1993. Effects of chemical environment on the solubility and incorporation mechanism for hydrogen in olivine. *Physics and Chemistry of Minerals* 19:460-471.
46. Zhao, Y. H., S. B. Ginsberg, and D. L. Kohstedt. 2004. Solubility of hydrogen in olivine: dependence on temperature and iron content. *Contributions to Mineralogy and Petrology* 147:155-161.

47. Mosenfelder, J. L., N. I. Deligne, P. D. Asimow, and G. R. Rossman. 2006. Hydrogen incorporation in olivine from 2-12 GPa. *American Mineralogist* 91:285-294.
48. Grant, K., J. Ingrin, J. P. Lorand, and P. Dumas. 2007. Water partitioning between mantle minerals from peridotite xenoliths. *Contributions to Mineralogy and Petrology* 154:15-34.
49. Grant, K. J., R. A. Brooker, S. C. Kohn, and B. J. Wood. 2007. The effect of oxygen fugacity on hydroxyl concentrations and speciation in olivine: Implications for water solubility in the upper mantle. *Earth and Planetary Science Letters* 261:217-229.
50. Demouchy, S., S. D. Jacobsen, F. Gaillard, and C. R. Stern. 2006. Rapid magma ascent recorded by water diffusion profiles in mantle olivine. *Geology* 34:429-432.
51. Canil, D., and A. J. Bellis. 2007. Ferric iron in $CaTiO_3$ perovskite as an oxygen barometer for kimberlite magmas II: Applications. *Journal of Petrology* 48:231-252.
52. Peslier, A. H., A. B. Woodland, D. R. Bell, and M. Lazarov. 2010. Olivine water contents in the continental lithosphere and the longevity of cratons. *Nature* 467:78-81.
53. Grant, K. J., S. C. Kohn, and R. A. Brooker. 2007. The partitioning of water between olivine, orthopyroxene and melt synthesised in the system albite-forsterite-H2O. *Earth and Planetary Science Letters* 260:227-241.
54. Koch-Müller, M., S. S. Matsyuk, D. Rhede, R. Wirth, and N. Khisina. 2006. Hydroxyl in mantle olivine xenocrysts from the Udachnaya kimberlite pipe. *Physics and Chemistry of Minerals* 33:276-287.
55. Peslier, A. H., and J. F. Luhr. 2006. Hydrogen loss from olivines in mantle xenoliths from Simcoe (USA) and Mexico: Mafic alkalic magma ascent rates and water budget of the sub-continental lithosphere. *Earth and Planetary Science Letters* 242:302-319.
56. Kresten, P., and A. N. Dempster. 1973. The Geology of Pipe 200 and the Malibamatso Dyke Swarm. In *Lesotho Kimberlites*. P. H. Nixon, ed. Lesotho National Development Corporation. 172-179.
57. Cox, K. G., J. Gurney, and B. Harte. 1973. Xenoliths from the Matsoku Pipe. In *Lesotho Kimberlites*. P. H. Nixon, ed. Lesotho National Development Corporation. 76-91.
58. Kopylova, M. G., and P. Hayman. 2008. Petrology and textural classification of the Jericho kimberlite, northern Slave Province, Nunavut, Canada. *Canadian Journal of Earth Sciences* 45:701-723.
59. De Stefano, A., M. G. Kopylova, P. Cartigny, and V. Afanasiev. 2009. Diamonds and eclogites of the Jericho kimberlite (Northern Canada). *Contributions to Mineralogy and Petrology* 158:295-315.
60. Kovacs, I., H. S. C. O'Neill, J. Hermann, and E. H. Hauri. 2010. Site-specific infrared O-H absorption coefficients for water substitution into olivine. *American Mineralogist* 95:292-299.
61. Paterson, M. S. 1982. The determination of hydroxyl by infrared-absorption in quartz, silicate-glasses and similar materials. *Bulletin De Mineralogie* 105:20-29.

62. Gurney, J. J., P. R. Hildebrand, J. A. Carlson, Y. Fedortchouk, and D. R. Dyck. 2004. The morphological characteristics of diamonds from the Ekati property, Northwest Territories, Canada. *Lithos* 77:21-38.
63. Dohmen, R., H. W. Becker, and S. Chakraborty. 2007. Fe-Mg diffusion in olivine I: experimental determination between 700 and 1,200 °C as a function of composition, crystal orientation and oxygen fugacity. *Physics and Chemistry of Minerals* 34:389-407.
64. Hurwitz, S., and O. Navon. 1994. Bubble nucleation in rhyolitic melts - experiments at high-pressure, temperature, and water-content. *Earth and Planetary Science Letters* 122:267-280.
65. Edwards, B., and J. K. Russell. 2009. Xenoliths as magmatic 'menthos'© (sic). *American Geophysical Union Joint Assembly*. American Geophysical Union, Toronto, Canada.
66. Canil, D., and Y. Fedortchouk. 1999. Garnet dissolution and the emplacement of kimberlites. *Earth and Planetary Science Letters* 167:227-237.
67. Shewmon, P. G. 1963. *Diffusion in Solids*. McGraw-Hill Book Company, Inc., New York.
68. Downes, P. J., J. A. Wartho, and B. J. Griffin. 2006. Magmatic evolution and ascent history of the Aries micaceous kimberlite, Central Kimberley Basin, Western Australia: Evidence from zoned phlogopite phenocrysts, and UV laser Ar-40/Ar-39 analysis of phlogopite-biotite. *Journal of Petrology* 47:1751-1783.
69. Kopylova, M. G., S. Matveev, and M. Raudsepp. 2007. Searching for parental kimberlite melt. *Geochimica Et Cosmochimica Acta* 71:3616-3629.
70. Grütter, H. S., J. J. Gurney, A. H. Menzies, and F. Winter. 2004. An updated classification scheme for mantle-derived garnet, for use by diamond explorers. *Lithos* 77:841-857.
71. Dawson, J. B., and J. V. Smith. 1975. Occurrence of diamond in a mica-garnet lherzolite xenolith from kimberlite. *Nature* 254:580-581.
72. Luth, R. W. 2009. The activity of silica in kimberlites, revisited. *Contributions to Mineralogy and Petrology* 158:283-294.
73. Mitchell, R. H. 2004. Experimental studies at 5-12 GPa of the Ondermatjie hypabyssal kimberlite. *Lithos* 76:551-564.
74. Costa, F., and S. Chakraborty. 2008. The effect of water on silicon and oxygen diffusion rates in olivine and implications for the transport properties and processes in the upper mantle. *Physics of the Earth and Planetary Interiors* 166:11-29.
75. Andersen, D. J., and D. H. Lindsley. 1981. A valid Margules formulation for an asymmetric ternary solution - revision of the olivine-ilmenite thermometer, with applications. *Geochimica Et Cosmochimica Acta* 45:847-853.

APPENDIX 1: SENSITIVITY OF DIFFUSION MODELING RESULTS TO PROFILE WIDTH

This appendix describes the sensitivity of $r_{A_{int}}$ calculated from the diffusion models to profile length, *h* (*i.e.*, grain size). Figure A1 compares $r_{A_{int}}$ *v. t* curves at three different values of *h* (1, 2, and 5 mm). At a constant temperature (*T* = 1100 °C in Figure A1) and crystallographic direction (*c* axis in Figure A1), the quantity $r_{A_{int}}$ varies similarly for the three *h* values at short durations. Calculated $r_{A_{int}}$ is identical for the three curves until ~100 min (Fig. A1 A), at which point the *h* = 1 mm curve begins to level off to a higher asymptote than the other curves (Fig. A1 B). The *h* = 1 mm condition approaches an asymptote of 0.23, whereas the 2 and 5 mm conditions approach 0.12 and 0.05, respectively. Curves corresponding to high *h* approach their asymptotes more gradually than low *h* curves. Values of $r_{A_{int}}$ are more sensitive to *h* where *h* is small; $r_{A_{int}}$ values for the 1 and 2 mm curves diverge more greatly than they do for the 2 and 5 mm curves. The 2 mm curve provides a reasonable model parameter for comparison with measured data because most crystals analyzed in this study fall between diameters of 1 and 5 mm, and some crystals from each xenolith have diameters of ~2 mm. However, the choice of *h* value may matter little for comparison with natural data, because the initial changes of $r_{A_{int}}$, which are the most relevant for such comparisons, are similar for the full range of *h* tested.

I assume that the models of Figure 4.2 are similarly sensitive to *h* as the model in Figure 4.1 despite the different calculations involved, because both models produce identical results in the anhydrous condition (equilibrium concentration [*Ceq*] = 0 in Figure 4.2). Changes in $r_{A_{int}}$ over time for $C_{eq} > 0$ at variable *h* should produce smaller divergences than those illustrated by Figure A1, because the difference between the initial concentration (C_0) and C_{eq} are smaller for all $C_{eq} \neq 0$ explored in this study.

ELECTRONIC APPENDICES

Electronic appendices are available online at *http://dalspace.library.dal.ca*. They include electron microprobe data, integrated absorbance *v*. position in crystal data, model parameters used, diffusion model data outputs, and raw spectra.

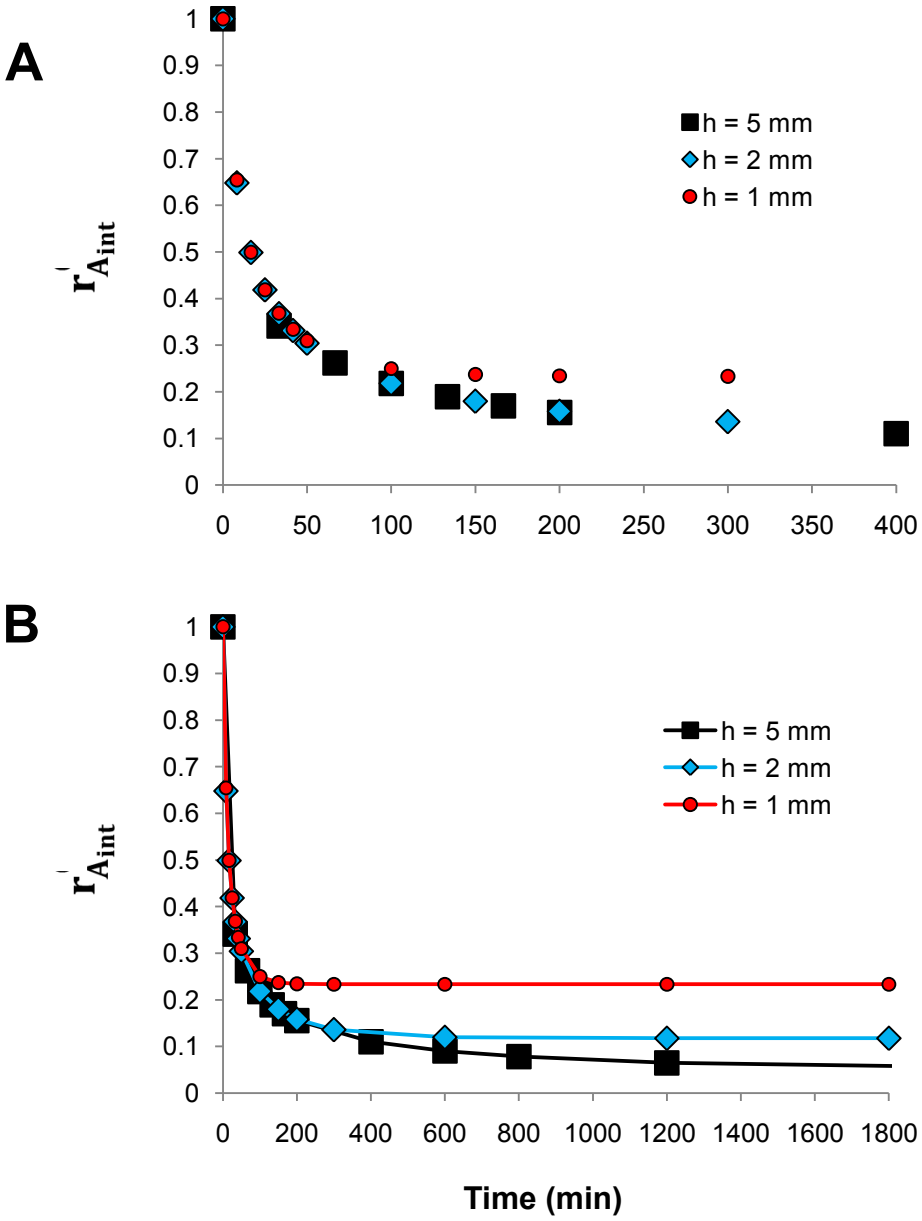

Figure A1: Sensitivity of model rim:core H-zonation ratios to model profile width. The *y* axis shows the rim:core intensity ratio, $r_{A_{int}}$. Different profile widths (h) produce similar trends in the early stages of the model, but approach different asymptotes. (**A**) Close-up view of early model times. (**B**) View at extended model times.